



# **NAVAL POSTGRADUATE SCHOOL**

**MONTEREY, CALIFORNIA**

## **THESIS**

**DIRECT IMAGING OF MINORITY CHARGE CARRIER  
TRANSPORT IN TRIPLE JUNCTION SOLAR CELL  
LAYERS**

by

Ted Jonathan Mills

December 2006

Thesis Advisor:  
Second Reader:

Nancy Haegel  
Sherif Michael

**Approved for public release; distribution is unlimited**

THIS PAGE INTENTIONALLY LEFT BLANK

<b>REPORT DOCUMENTATION PAGE</b>			Form Approved OMB No. 0704-0188	
Public reporting burden for this collection of information is estimated to average 1 hour per response, including the time for reviewing instruction, searching existing data sources, gathering and maintaining the data needed, and completing and reviewing the collection of information. Send comments regarding this burden estimate or any other aspect of this collection of information, including suggestions for reducing this burden, to Washington headquarters Services, Directorate for Information Operations and Reports, 1215 Jefferson Davis Highway, Suite 1204, Arlington, VA 22202-4302, and to the Office of Management and Budget, Paperwork Reduction Project (0704-0188) Washington DC 20503.				
<b>1. AGENCY USE ONLY (Leave blank)</b>		<b>2. REPORT DATE</b> December 2006	<b>3. REPORT TYPE AND DATES COVERED</b> Master's Thesis	
<b>4. TITLE AND SUBTITLE:</b> Direct Imaging of Minority Charge Carrier Transport in Triple Junction Solar Cell Layers			<b>5. FUNDING NUMBERS</b>	
<b>6. AUTHOR(S)</b> Ted Jonathan Mills				
<b>7. PERFORMING ORGANIZATION NAME(S) AND ADDRESS(ES)</b> Naval Postgraduate School Monterey, CA 93943-5000			<b>8. PERFORMING ORGANIZATION REPORT NUMBER</b>	
<b>9. SPONSORING /MONITORING AGENCY NAME(S) AND ADDRESS(ES)</b> National Science Foundation Division of Materials Research (DMR)			<b>10. SPONSORING/MONITORING AGENCY REPORT NUMBER</b>	
<b>11. SUPPLEMENTARY NOTES</b> The views expressed in this thesis are those of the author and do not reflect the official policy or position of the Department of Defense or the U.S. Government.				
<b>12a. DISTRIBUTION / AVAILABILITY STATEMENT</b> Approved for public release; distribution is unlimited			<b>12b. DISTRIBUTION CODE</b>	
<b>13. ABSTRACT (maximum 200 words)</b> <p>An optical, contact-free method for measuring minority carrier diffusion lengths is developed and demonstrated for a range of semiconductor materials used in high efficiency triple junction solar cells. This method uses a Scanning Electron Microscope (SEM) coupled with an optical microscope. The diffusion lengths, combined with minority carrier lifetime measured via time-resolved photoluminescence, allow for the computation of minority charge carrier mobility.</p> <p>The technique uses images to extract diffusion length measurements from GaAs, InGaAs, and InGaP heterostructures at different SEM beam energies and probe currents. Excellent correlation between measurements shows the reproducibility of this technique. Diffusion lengths from 2-63 microns have been measured in a variety of GaAs, InGaAs, and InGaP samples. Effects of alloy ordering, doping, and lattice matching have been investigated.</p> <p>Several areas for further research are offered, including detailed radiation-damage mapping of solar cell layers. Further anisotropic studies of the solar cell layers are suggested to investigate the directional dependence of diffusion length within the InGaP heterostructures. Finally, new and emerging solar cell materials would benefit from this technique, allowing for the complete characterization of minority charge transport properties before growing an entire solar cell.</p>				
<b>14. SUBJECT TERMS</b> Solar Cells, Triple Junction Solar Cells, Semiconductor, Diffusion Length, Minority Charge Carrier, Transport Imaging, Minority Carrier Mobility			<b>15. NUMBER OF PAGES</b> 81	
			<b>16. PRICE CODE</b>	
<b>17. SECURITY CLASSIFICATION OF REPORT</b> Unclassified	<b>18. SECURITY CLASSIFICATION OF THIS PAGE</b> Unclassified	<b>19. SECURITY CLASSIFICATION OF ABSTRACT</b> Unclassified	<b>20. LIMITATION OF ABSTRACT</b> UL	

NSN 7540-01-280-5500

Standard Form 298 (Rev. 2-89)  
Prescribed by ANSI Std. Z39-18

THIS PAGE INTENTIONALLY LEFT BLANK

**Approved for public release; distribution is unlimited**

**DIRECT IMAGING OF MINORITY CHARGE CARRIER TRANSPORT IN  
TRIPLE JUNCTION SOLAR CELL LAYERS**

Ted Jonathan Mills  
Captain, United States Air Force  
B.S., Embry-Riddle Aeronautical University, 1997

Submitted in partial fulfillment of the  
requirements for the degree of

**MASTER OF SCIENCE IN APPLIED PHYSICS**

from the

**NAVAL POSTGRADUATE SCHOOL  
December 2006**

Author: Ted Jonathan Mills

Approved by: Nancy M. Haegel  
Thesis Advisor

Sherif Michael  
Co-Advisor

James H. Luscombe  
Chairman, Department of Physics

THIS PAGE INTENTIONALLY LEFT BLANK

## **ABSTRACT**

An optical, contact-free method for measuring minority carrier diffusion lengths is developed and demonstrated for a range of semiconductor materials used in high efficiency triple junction solar cells. This method uses a Scanning Electron Microscope (SEM) coupled with an optical microscope. The diffusion lengths, combined with minority carrier lifetime measured via time-resolved photoluminescence, allow for the computation of minority charge carrier mobility.

The technique uses images to extract diffusion length measurements from GaAs, InGaAs, and InGaP heterostructures at different SEM beam energies and probe currents. Excellent correlation between measurements shows the reproducibility of this technique. Diffusion lengths from 2-63 microns have been measured in a variety of GaAs, InGaAs, and InGaP samples. Effects of alloy ordering, doping, and lattice matching have been investigated.

Several areas for further research are offered, including detailed radiation-damage mapping of solar cell layers. Further anisotropic studies of the solar cell layers are suggested to investigate the directional dependence of diffusion length within the InGaP heterostructures. Finally, new and emerging solar cell materials would benefit from this technique, allowing for the complete characterization of minority charge transport properties before growing an entire solar cell.

THIS PAGE INTENTIONALLY LEFT BLANK



## TABLE OF CONTENTS

I.	INTRODUCTION.....	1
A.	SOLAR CELL MATERIAL DIFFUSION LENGTH STUDY .....	1
B.	PURPOSE OF THESIS .....	2
C.	MILITARY RELEVANCE .....	3
D.	THESIS OVERVIEW .....	4
II.	BACKGROUND.....	5
A.	TRIPLE JUNCTION SOLAR CELLS .....	5
B.	CHARGE CARRIERS IN SEMICONDUCTORS .....	8
C.	DIFFUSION, MOBILITY, AND LIFETIME .....	10
D.	LUMINESCENCE IN SEMICONDUCTORS.....	12
III.	EXPERIMENTAL APPROACH.....	15
A.	DIRECT DIFFUSION IMAGING .....	15
B.	EQUIPMENT .....	15
IV.	DIFFUSION LENGTH EXTRACTION STUDIES .....	21
A.	DIFFUSION LENGTH EXTRACTION METHODOLOGIES .....	21
1.	1/Slope Technique .....	22
2.	Diffusion Length Look-up via Model Slope Matching.....	28
B.	TRIPLE JUNCTION SOLAR CELL MATERIALS.....	31
1.	Indium Gallium Phosphide Double Heterostructures.....	32
2.	Indium Gallium Arsenide Double Heterostructures.....	36
3.	Experimental Results .....	37
V.	CONCLUSION AND SUGGESTION FOR FURTHER RESEARCH.....	43
A.	SUMMARY AND CONCLUSION .....	43
B.	SUGGESTIONS FOR FURTHER RESEARCH .....	44
1.	Crystallographic Directionality Dependence of Diffusion Length.....	44
2.	Radiation Effects on Diffusion Length.....	47
APPENDIX A.	ANISOTROPIC DIFFUSION LENGTH MEASUREMENT MATLAB CODE (ANISOTROPIC.M) .....	51
APPENDIX B.	T-FACTOR DIFFUSION LENGTH MEASUREMENT MATLAB FUNCTION (TFACTOR.M) .....	59
APPENDIX C.	T-FACTOR DIFFUSION LENGTH MEASUREMENT DATA FILE (TFACTORDATA.CSV) .....	61
	LIST OF REFERENCES.....	63
	INITIAL DISTRIBUTION LIST .....	65

THIS PAGE INTENTIONALLY LEFT BLANK

## LIST OF FIGURES

Figure 1.	Triple-Junction Solar Cell Absorption Efficiency (From: [4]).	6
Figure 2.	Two Stacked Solar Cell Layers without and with a Tunnel Junction.	7
Figure 3.	Typical Layers of a Triple-Junction Solar Cell.	8
Figure 4.	Electron-Hole Creation via Photon Absorption and Recombination.	12
Figure 5.	InGaP Emission Spectrum via CL Excitation.	13
Figure 6.	JEOL 840A SEM with Modified Stage and Optical Microscope.	16
Figure 7.	Apogee 2184 x 1472 Cooled CCD.	16
Figure 8.	Schematic of Transport Imaging Components.	17
Figure 9.	Image of n <sup>+</sup> InGaP in Picture Mode (140 $\mu\text{m}$ x 160 $\mu\text{m}$ ).	17
Figure 10.	Image of doped p-type GaAs in Spot Mode (160 $\mu\text{m}$ x 160 $\mu\text{m}$ ).	18
Figure 11.	Image and Horizontal Line Profile of doped p-type GaAs.	19
Figure 12.	Modeled Distribution of Minority Charge Carriers (After: [11]).	23
Figure 13.	Error of Estimated Diffusion Length as a Function of Distance from Charge Generation Center (After: [11]).	23
Figure 14.	Image of Luminescence Distribution in GaAs (245 $\mu\text{m}$ x 210 $\mu\text{m}$ ).	24
Figure 15.	Normalized Intensity as a Function of Position.	25
Figure 16.	Semi-logarithmic Plot of Normalized Intensity as a Function of Position.	25
Figure 17.	Semi-logarithmic Plot of Normalized Intensity as a Function of Position and Linear Regression Lines for Slope extraction.	26
Figure 18.	Experimental and Modeled Slope Data Comparison.	28
Figure 19.	Modeled Slope values versus Diffusion Length and Diffusion Length Extraction from Experimental Data.	29
Figure 20.	Two-Parameter Fit of Model to Experimental Data on GaAs Sample.	31
Figure 21.	Schematic and Band Diagram of Double Heterostructure.	32
Figure 22.	I-V Curves for Ge, Si, GaAs, and InGaP Cells Under AM0 Solar Illumination (From: [4]).	33
Figure 23.	Zinc Blende Cubic Crystal Structure (From: [1]).	34
Figure 24.	Ordered and Disorder Domains of CuPt ordering in III-V Semiconductor Alloys (From: [15]).	34
Figure 25.	CL Spectra of doped MM and n <sup>+</sup> LM InGaP.	35
Figure 26.	CL Spectra of GaAs and 1%-In InGaAs.	37
Figure 27.	Distribution of Luminescence of Samples 564-1Tb, 24-1Tb, 24-1Mb and 23-1Mb under SEM Spot Mode Excitation (all pictures 160 $\mu\text{m}$ x 160 $\mu\text{m}$ ).	38
Figure 28.	Modeled and Experimental Data of 564-1Tb, 24-1Tb, 24-1Mb and 23-1Mb.	39
Figure 29.	Images (250 $\mu\text{m}$ x 275 $\mu\text{m}$ ) of Sample 24-1Tb taken on 28 September and 3 October Respectively.	44
Figure 30.	Output Plots of Matlab Code 'anisotropic.m'.	46

Figure 31.	Image ( $700\mu m$ x $500\mu m$ ) of Luminescence from Radiation Damaged GaAs with SEM in Picture Mode. ....	47
Figure 32.	Spot Mode Images ( $216\mu m$ x $200\mu m$ ) of Luminescence Distribution Changes in Damaged (A), Undamaged (C), and between the Damaged/Undamaged Regions (B) of GaAs. ....	48
Figure 33.	Line Profiles of Spot Images in Undamaged and Radiation Damaged GaAs. ....	49
Figure 34.	Semi-logarithmic Plot of Normalized Intensity versus Position for Luminescence of Figure 32.B. ....	49

## LIST OF TABLES

Table 1.	Results of 1/Slope Technique on GaAs Sample.....	27
Table 2.	Results of Slope Matching Technique on GaAs Sample. ....	29
Table 3.	InGaP Double Heterostructures Sample Parameters.....	36
Table 4.	InGaAs Double Heterostructures Sample Parameters. ....	37
Table 5.	Diffusion Length Measurement Results for all Samples. ....	40
Table 6.	Results of Anisotropic Diffusion Length Measurements in InGaP. ....	46
Table 7.	Diffusion Length Measurements of Radiation Damaged GaAs. ....	50

THIS PAGE INTENTIONALLY LEFT BLANK

## **ACKNOWLEDGMENTS**

This work was supported by the National Science Foundation through Grants DMR-0203397 and DMR-0526330.

My appreciation and thanks goes to Dr. Nasser Karam, Dr. Richard King, and Dr. Hojun Yoon from Spectrolab, Inc. Without their expertise, knowledge, and samples, this work would not have been accomplished. Additionally, much of the theoretical model work is attributed to Mike Talmadge of Fairfield University; much of my work was adapted from his work. Additional thanks go to Wladek Walukiewicz and Kin Man Yu of Lawrence Berkeley National Laboratory for helpful discussions and performing proton irradiation respectively. I also would like to thank my co-advisor, Dr. Sherif Michael, and Dr. Gamani Karunasiri for their excellent support and energizing me in solar cell and semiconductor technologies.

Special thanks are warranted to my thesis advisor, Dr. Nancy Haegel. Her knowledge is inspiring and most helpful, but more importantly, her enthusiasm for our research motivated me above all else. Working with her, it is hard not to get excited yourself when obtaining new and interesting experimental results. I can not imagine finding better thesis advisor and colleague for my work here at NPS.

Finally, I am constantly amazed at the love and support I receive from my wife, Rebecca. I love you and thank you for your support during my studies here at NPS.

THIS PAGE INTENTIONALLY LEFT BLANK



# **I. INTRODUCTION**

## **A. SOLAR CELL MATERIAL DIFFUSION LENGTH STUDY**

The need for power for space applications is a primary driving force for the use and continued improvement of solar cell technology. Although there are other power options available for space applications, some provide power for limited amounts of time (batteries, fuel cells), until the energy stored is depleted, while others require radioactive material for long-term power generation. Only solar cell technology takes the unlimited amount of energy provide by the sun and coverts it into usable electrical energy. However, with the trend of increasingly higher power requirements on-orbit and the growing need for environmental-friendly, low-cost terrestrial power requirements, the demand for highly efficient and cost effective solar cells has increased dramatically.

Solar cells are photovoltaic devices that are dependent on charge collection in the depletion region of a semiconductor p-n junction. Typical solar cells have a very narrow and more heavily doped n-type region, which results in the depletion region extending primarily into a thicker p-type region. Most of the photons entering the junction are absorbed within the p-type layer, creating electron-hole pairs [1]. This premise is true for Silicon (Si) solar cells as well as most binary or ternary compound solar cells that use element III-V combinations, such as Gallium Arsenide (GaAs), Indium Gallium Arsenide (InGaAs or GaInAs), and Indium Gallium Phosphide (InGaP or GaInP). Regardless of the solar cell type, one of the largest contributing factors to optimized solar cell operations is the efficient collection of charge produced by the absorbed light and transport of that charge out of the solar cell. To accomplish that goal, the electrons produced in the p-type parallel structure layer need to be transferred to the n-type layer. The electrons, as the minority charge carriers in the p-type layer, must have a diffusion length sufficient to allow them to diffuse to the depletion region, where they will be transported into the n-type layer by the built-in electric field within the depletion region [1].

The minority charge carrier diffusion length in the p-type layer of a solar cell, therefore, is a key parameter in determining final device performance. The ability to efficiently operate depends on the diffusion length being larger than the p-type layer's thickness, or the electron can be lost due to recombination with excess holes. In advanced solar cells, there are multiple p-n junctions, each absorbing a different part of the solar spectrum. The minority charge carrier diffusion lengths within each p-type layer of the multiple p-n junctions must be fully characterized and optimized for state-of-the-art performance.

## **B. PURPOSE OF THESIS**

The goal of this thesis is to develop and demonstrate an optical, contact-free technique for measurement of the diffusion length of minority charge carriers in the p-type layers of a triple junction solar cell. In combination with other techniques, such as time resolved photoluminescence (TRPL), additional material properties extracted via other methods allow the full characterization of the key material charge transport parameters—mobility, lifetime and diffusion length. Although this can not be done from a full solar cell directly, the various p-type layers of the solar cell have been grown in two dimensional (2D) heterostructures, allowing for well controlled individual layer characterization and the experimental extraction of the diffusion length. The ease of extracting these parameters and the potential to characterize various layers of a solar cell before growing the complex multi-junction cell shows the benefit of using such a technique.

The measurement technique can also easily measured changes in diffusion length due to radiation damage and directionality preferences of diffusion length parameters. Results are presented from the following experiments: diffusion measurements in 2D heterostructure samples of InGaP, GaAs, and InGaAs, preliminary diffusion length measurements in radiation damaged GaAs, and preliminary diffusion length anisotropy in InGaP. These measurements were performed using a Scanning Electron Microscope (SEM)

with a modified liquid helium cooled stage and thermoelectrically cooled silicon charge coupled device (CCD) camera in the Physics Department at the Naval Postgraduate School (NPS).

### **C. MILITARY RELEVANCE**

Earth orbiting satellites at low-Earth to geosynchronous orbits, which include all military satellites, employ solar cells as their power source because of reliability [2]. Although there are other means of power generation (fuel cells, radio-isotope thermal generators), only solar cells provide reliable, low-power over long time periods for relatively low cost and no added complexities of dealing with radioactive materials. The military's reliance on military and commercial satellite communications, navigation, and Intelligence, Surveillance, and Reconnaissance (ISR) has increased dramatically within the last couple of decades. The increased reliance and the relatively long acquisition process of new space assets have led to the use of current space-borne assets well beyond their design lifetime. The solar panels on these satellites were designed to provide enough power at the satellite's end-of-life (EOL); the constant radiation environment to which the satellite is exposed continues to reduce the effectiveness of the solar cells' ability to produce power.

The ability to directly measure diffusion length variations in the layers of the solar cell as a function of radiation damage is important in designing future, radiation resistant solar cells. The optical characterization and measurement technique is very sensitive to radiation damage of the crystalline structure of the solar cells' layers. A full characterization of the key material charge transport parameters with the diffusion length measurement technique and TRPL enables solar cell manufacturers to understand the radiation effects of the solar cell at an early stage of the design process.

The military's reliance on space assets has also spawned efforts to design and field smaller, more responsive satellites to support the combatants within a specific area of interest. This push for operationally responsive space assets is

leading to development of smaller satellites that can be launched on short notice with smaller, cheaper launch vehicles. With volume and weight a premium on small launch vehicles, the need for lightweight, very efficient solar cells is apparent. New techniques, such as the transport imaging developed here, continually add to the development of more efficient and more cost effective solar cell technologies.

#### **D. THESIS OVERVIEW**

Chapter I provides an introduction to the thesis, explaining the diffusion length extraction study for solar cell layers, outlining the purpose of the thesis, and discussing the military relevance. A brief but necessary background of solar cells, with emphasis on triple junction cells, is given in Chapter II. Additionally, charge carriers in semiconductors, luminescence in semiconductors, and diffusion, mobility, and lifetime of charge carriers are reviewed. Chapter III explains the experimental approach for direct diffusion imaging and the equipment used. The experimental methodologies to extract diffusion length are detailed in Chapter IV. Details of the various layers of the triple junction solar cell are discussed and the experimental results are presented. Finally, Chapter V summarizes the results and presents further research areas, including preliminary results on radiation damage and dependence of diffusion length on crystallographic direction.

## **II. BACKGROUND**

### **A. TRIPLE JUNCTION SOLAR CELLS**

The push towards triple junction solar cells has always been motivated by a desire to convert as much of the sunlight incident on the solar cell into electricity as possible. The first solar cells made of Si only convert a portion of the solar spectrum into electricity, with a threshold for absorption determined by the band-gap of Si. Photons with energy less than the Si band-gap don't have sufficient energy to excite the electron from the valence band to the conduction band. Photons that have energy equal to the band-gap of Si do have enough energy to excite electrons into the conduction band, but the density of states of electrons near the top of the valence band is low and efficient absorption of photons increases as the photon energy increases. However, higher energy photons have more energy than required to excite the electron to the conduction band, and the additional energy of the photon is converted into heat, increasing lattice vibrations within the semiconductor crystal. This additional heat reduces the electron lifetime and diffusion length in the conduction band. This leads to a decrease in efficiency of the solar cell.

The goal of a multi-junction solar cell is to stack different solar cells on top of each other. The top cell absorbs the higher energy photons. Photons with energy less than that layer's band-gap pass through the cell as though that layer is transparent and are absorbed in the cell underneath. This method allows for more efficient absorption of the solar spectrum while reducing the amount of wasted energy that is converted into heat. The most common type of multi-junction solar cell is an InGaP/GaAs/Ge triple-junction solar cell [3]. Figure 1 shows the absorption efficiency of each layer of the triple-junction cell, and the overall absorption efficiency of the solar cell as a function of wavelength. The figure also shows the solar spectrum encountered in space, commonly labeled as AM0. This figure illustrates a more efficient use of the solar spectrum by a triple-junction solar cell compared to a single-junction solar cell, such as a GaAs single-junction cell.

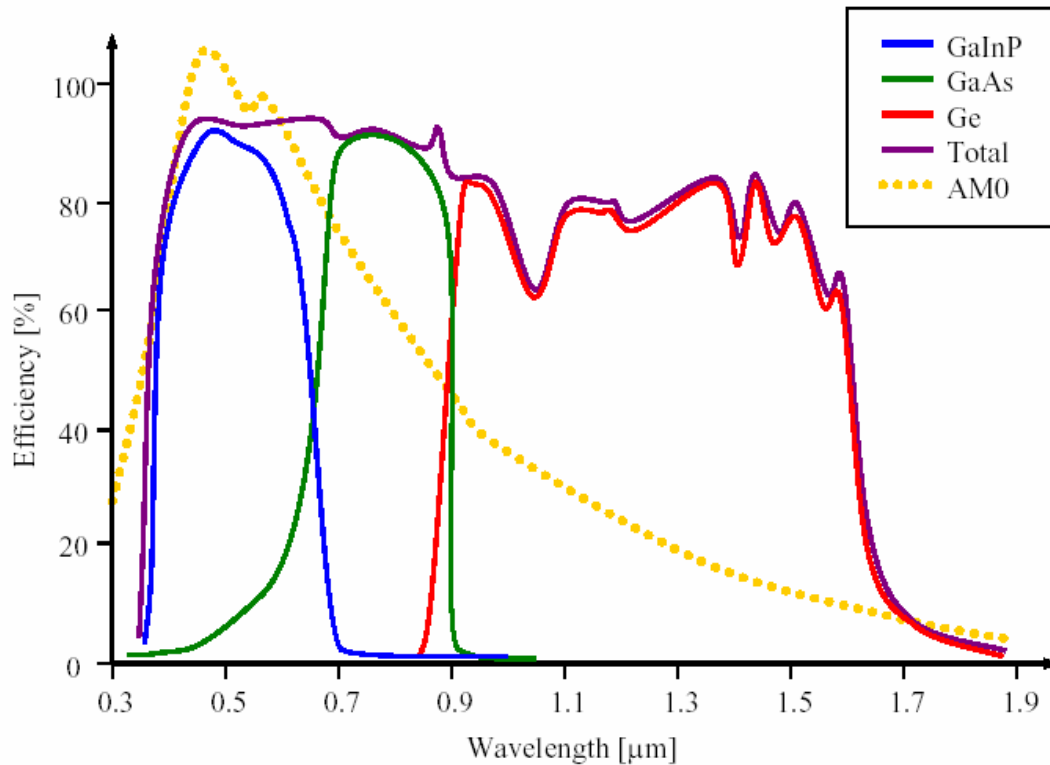


Figure 1. Triple-Junction Solar Cell Absorption Efficiency (From: [4]).

Although triple-junction solar cells do provide for more efficient use of the solar spectrum, there are problems that must be overcome to manufacture a working triple-junction solar cell. The first problem is that each solar cell is an n-on-p junction. If you stack two solar cells on top of each other, a p-on-n junction will form between the cells, creating a parasitic depletion layer prohibiting the desired flow of charge, as shown in Figure 2. The solution to this problem is to insert a tunnel junction between the two cells. This requires that p-type and n-type layers that are more heavily doped than the solar cell layers be placed in between the two cells. These two heavily doped layers set up a tunneling field that allows for charge to flow between the two layers, as shown in Figure 2. Although this solution is not ideal as there are some losses, this is the best alternative for the transport of charge through a multi-junction solar cell.

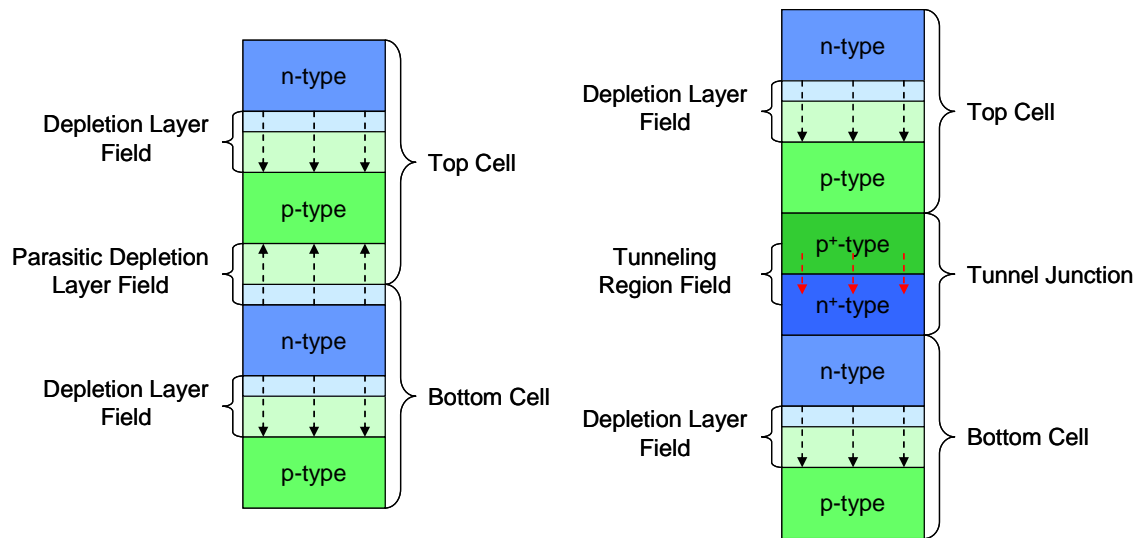


Figure 2. Two Stacked Solar Cell Layers without and with a Tunnel Junction.

Another enhancement added to a multi-junction solar cell is to increase the efficiency of moving the minority charge carriers (electrons) in the p-type region of the solar cell towards the depletion layer. Typically, the p-type regions are much thicker than the n-type regions, and electrons far away from the depletion layer will not be influenced by the depletion layer electric field. The addition of a more heavily doped p-type region at the bottom of the cell creates another internal electric field that will repel electrons from the bottom of the cell towards the depletion region. This additional layer is called a Back Surface Field (BSF) layer.

Finally, another approach used to increase the efficiency of a multi-junction solar cell is to decrease surface recombination in between the solar cell layers. Multi-junction cells are typically made up of different binary and ternary alloys, and each of these alloys has different lattice spacing between the atoms in the crystal. When two alloys of different lattice spacing are grown on top of each other, there is a lattice mismatch between the two alloys. This mismatch causes defects between the two layers, decreasing efficiency of charge transport across the two layers by allowing the electrons to recombine via the associated defect states, decreasing the current flow through the cell. Minimizing the lattice strain or matching the two layers' lattice spacing will reduce these recombination

paths. To a certain extent, the alloy's exact composition can be changed to modify the lattice spacing of one alloy to match the other's lattice spacing. Another way to decrease these interface losses is to insert an additional layer in between the two mismatched layers, creating a gradient that smoothes out the lattice mismatch between the two layers [4]. This layer, called a window, decreases surface recombination between the layers, but is thin enough to allow most photons through without absorption. Figure 3 shows a typical triple-junction solar cell with the tunnel junctions, BSF, and window layers, as well as an additional layer for the top contact and an Anti-Reflective Coating (ARC).

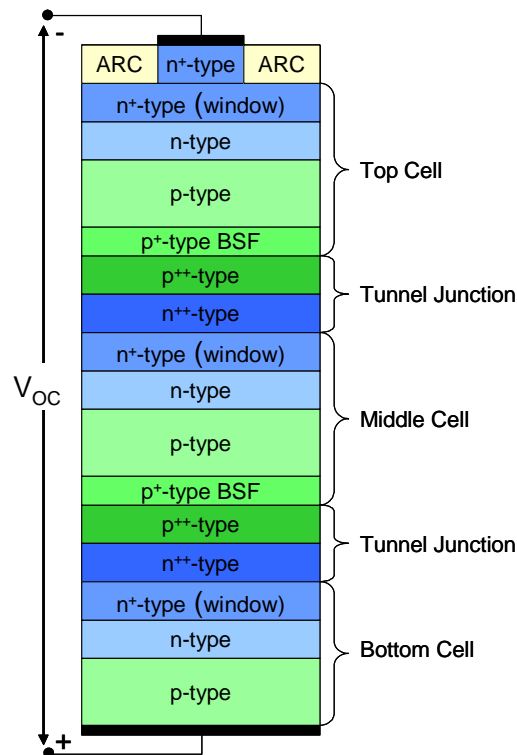


Figure 3. Typical Layers of a Triple-Junction Solar Cell.

## B. CHARGE CARRIERS IN SEMICONDUCTORS

Within the crystalline structure of a semiconductor, inter-atomic interactions lead to the formation of discrete energy bands, which include both allowed and forbidden energy levels [5]. The lower energy bands, called the valence bands, are filled with electrons bound to atoms within the crystal. The valence band is separated from the conduction band by a region of forbidden



energy levels called the band-gap. Electrons that gain enough energy can be removed from the valence band and transition to the conduction band. Once there, the electron is free to move within the conduction band. At the same time, a vacancy is created within the valence band where the electron used to be. This vacancy, called a hole, can be filled by adjacent electrons within the valence band. This gives the appearance of the hole moving within the valence band. Hence, holes are treated as positive charge carriers within the valence band, while electrons are negative charge carriers within the conduction band.

An undoped semiconductor in equilibrium will have equal amounts of electrons and holes due to thermal excitation across the band-gap. This is due to a hole being created every time an electron is excited from the valence band to the conduction band. The equation that governs carrier concentration in an undoped, or intrinsic, semiconductor is,

$$n_i^2 = n_o p_o \quad (1)$$

where  $n_i$  is the average intrinsic carrier concentration, which is constant for a certain temperature,  $n_o$  is the electron charge carrier concentration, and  $p_o$  is the hole charge carrier concentration.

Semiconductors can be doped with either donor impurities, atoms which possess one extra electron than the number needed to bond with the atoms around it in the crystal, or acceptor impurities, atoms which lack one electron needed to completely bond with the atoms around it in the crystal. Semiconductors doped with donor atoms will have excess electrons that will be free to move in the conduction band and are called n-type semiconductors. Semiconductors doped with acceptor atoms will have excess holes in the valence band and are called p-type semiconductors. In p-type materials, the doping concentration,  $N_A$ , is typically larger than the average hole charge carrier concentration of intrinsic semiconductors. This leads to Equation 1 becoming

$$n_i^2 = n_{po} N_A = n_{po} p_{po} \quad (2)$$

where  $n_{po}$  is the electron concentration in p-type material (minority charge carrier concentration) and  $p_{po}$  is the hole concentration in p-type material (majority charge carrier concentration).

Under external excitation, such as photons or an electron beam, electron hole pairs are produced in the semiconductor, and Equation 1 (for intrinsic) or Equation 2 (for p-type) does not hold true anymore. Specifically, in p-type semiconductors under external excitation, the relative amount of change in majority charge carriers is small, but is large for minority charge carriers. Therefore, non-equilibrium semiconductor electrical properties are often determined by the behavior of minority charge carriers. Minority charge carrier parameters are important physical properties in designing efficient solar cells [6].

### C. DIFFUSION, MOBILITY, AND LIFETIME

Diffusion in a semiconductor material is the migration of charge carriers, whether electrons or holes, due to a concentration gradient [5]. The diffusion coefficient ( $D$ ), given by the Einstein relation, is a measure of ease with which the charge carriers can diffuse through the material:

$$D = \frac{kT\mu}{e} \quad (3)$$

where  $k$  is Boltzmann's constant,  $T$  is the temperature, and  $\mu$  is the mobility. It is important to note that there are separate mobility values for electrons and holes which reflect differences in band structure and effective mass. This is more readily apparent when considering charge carrier drift, which is charge carrier motion due to an applied bias. Under drift, the current density within a uniformly doped sample is:

$$J = env_{de} + epv_{dh} \quad (4)$$

where  $v_{de}$  and  $v_{dh}$  are the electron and hole drift velocities respectively for an applied, one-dimensional electric field ( $E$ ). These drift velocities are defined as:

$$v_{de} = \frac{e\tau_e}{m_e^*} E \text{ \& } v_{dh} = \frac{e\tau_h}{m_h^*} E \quad (5)$$

where  $\tau_e$  and  $\tau_h$  is the mean free scattering time, or lifetime of the electrons and holes, while  $m_e^*$  and  $m_h^*$  are the effective masses of the electron and holes. In Equation 5, the constant of proportionality between the electric field and the drift velocity is defined as the mobility. Therefore, the mobility for electrons and holes is defined as:

$$\mu_e = \frac{e\tau_e}{m_e^*} \text{ \& } \mu_h = \frac{e\tau_h}{m_h^*} \quad (6)$$

showing the difference in electron and hole mobility.

The diffusion length is the semiconductor parameter measured by the technique developed in this thesis. The diffusion length is the average length a charge carrier, electron or hole, diffuses before it recombines. The diffusion length ( $L_{Diff}$ ) is given by:

$$L_{Diff} = \sqrt{D\tau} = \sqrt{\frac{\mu\tau kT}{e}} \quad (7)$$

with all the variables previously defined. As indicated in Equation 7, the three main parameters that determine a semiconductor's electrical properties are carrier diffusion length, mobility, and lifetime.

Time-resolved photoluminescence (TRPL) is a standard technique used to measure excess charge carrier lifetime. TRPL uses fast detectors to measure the time dependence of the luminescence intensity following a pulsed laser excitation. The time constant  $\tau$  for the intensity decay in the form of  $I \approx I_0 e^{-t/\tau}$  is the charge carrier lifetime.

Charge carrier mobility has been measured historically using the Haynes-Shockley technique [7]. Charge carriers are injected at one end of the semiconductor and moved across the semiconductor under the influence of an electric field. Knowing the transit distance, and the transit time via an oscilloscope, the transit velocity can be calculated. Since the mobility is simply

the proportionality constant between the electric field and velocity, the mobility can be calculated. This technique requires the addition of contacts on the sample to set up an electric field. Additionally, material uniformity must be assumed since the mobility measurement is averaged over the entire area between the contacts.

The technique developed and refined in this thesis measures the diffusion length of the semiconductor sample without the need for electric field or contacts. Using our technique in combination with other techniques, the diffusion length, lifetime and mobility can be found, allowing full characterization of the key material charge transport parameters.

#### D. LUMINESCENCE IN SEMICONDUCTORS

An electron that is excited, either thermally or from an external source (photon or electron beam), will transition from the valence band to the conduction band. There, the electron can move about freely and contribute to the electrical conductivity. Eventually, the electron can recombine with a free hole in the valence band, emitting a photon with energy equal to the band-gap. These processes are illustrated in Figure 4, which shows the energy levels of the valence band ( $E_v$ ), the conduction band ( $E_c$ ), the band-gap ( $E_g$ ), and the width of the conduction band ( $\chi$ ), also known as the electron affinity.

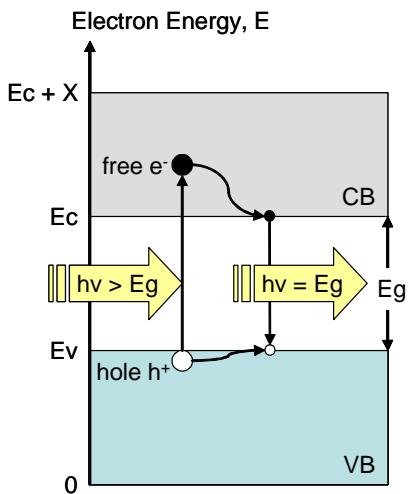


Figure 4. Electron-Hole Creation via Photon Absorption and Recombination.

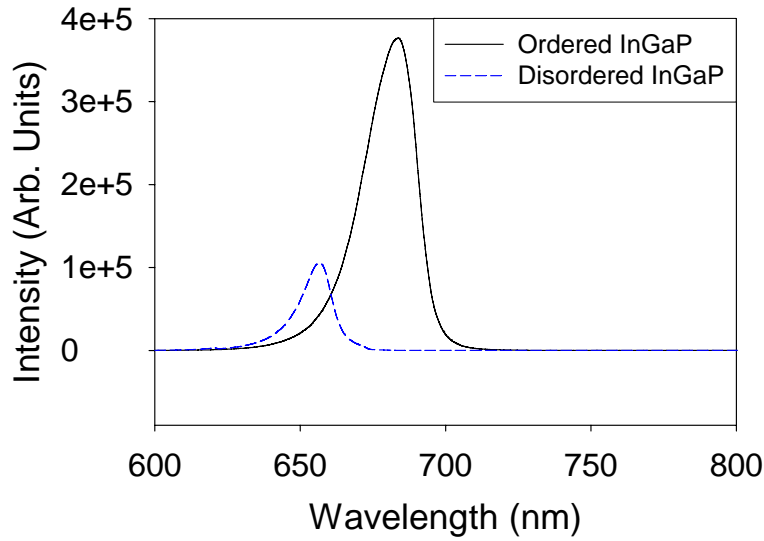


Figure 5. InGaP Emission Spectrum via CL Excitation.

The electron-hole recombination process illustrated in Figure 4 is the key process used in the technique developed to measure the diffusion length. In direct band-gap materials, such as the materials used in solar cell layers, the recombination is mostly radiative. Figure 5 show the emission spectrum of the ordered and disordered not intentionally doped (nid) p-type InGaP samples. This electromagnetic radiation emission of band-edge light by electron-hole recombination is an important form of luminescence in semiconductor materials. The collection of these emitted photons while maintaining the spatial information of the luminescence source is key for the technique developed to extract the diffusion length.

THIS PAGE INTENTIONALLY LEFT BLANK

### **III. EXPERIMENTAL APPROACH**

#### **A. DIRECT DIFFUSION IMAGING**

The direct diffusion imaging technique presented in this thesis illustrates a way to experimentally obtain the diffusion length of minority carriers in semiconductor materials. The focus in this work is on the p-type layers of a triple junction solar cell. The technique directly images the radiative recombination of electron-hole pairs. This process is similar to conventional cathodoluminescence (CL), with an electron beam as the external source for generating electron-hole pairs. The production and radiative recombination processes of electron-hole pairs are at steady-state, and the electron beam is held over a fixed position on the sample. In transport imaging, the spatial information of the electron-hole pair recombination is retained, and not lost as in standard CL [8]. This allows for the image capture of any distribution of the luminescence within the sample due to diffusion of electrons, so that one can observe the transport of the minority charges. The simplicity of this method allows for diffusion length measurements without any additional sample preparation or need for contact points on the sample.

#### **B. EQUIPMENT**

The system used consists of a JEOL 840A SEM with an internal optical microscope to capture the images. A modified, liquid helium-cooled SEM stage from Oxford Instruments allows for the sample to be studied at temperatures from 5 – 300K. Figure 6 shows the SEM with the modified stage and the optical microscope attached.



Figure 6. JEOL 840A SEM with Modified Stage and Optical Microscope.

The optical detector used on the optical microscope is a thermoelectrically-cooled Apogee silicon charge coupled device (CCD) camera with a 2184 x 1472 pixel array. The CCD is cooled to about  $-20^{\circ}\text{C}$  during operation for noise reduction and collects unfiltered light from 400 to 1100 nm. The CCD pixel size is  $8.6 \times 8.6 \mu\text{m}$  and the resulting imaging resolution is approximately  $0.4 \mu\text{m}/\text{pixel}$ . This resolution is close to the diffraction limit for the observation of luminescence from room temperature GaAs at 870 nm. The CCD camera is shown in Figure 7 while Figure 8 shows a schematic of the entire system.



Figure 7. Apogee 2184 x 1472 Cooled CCD.



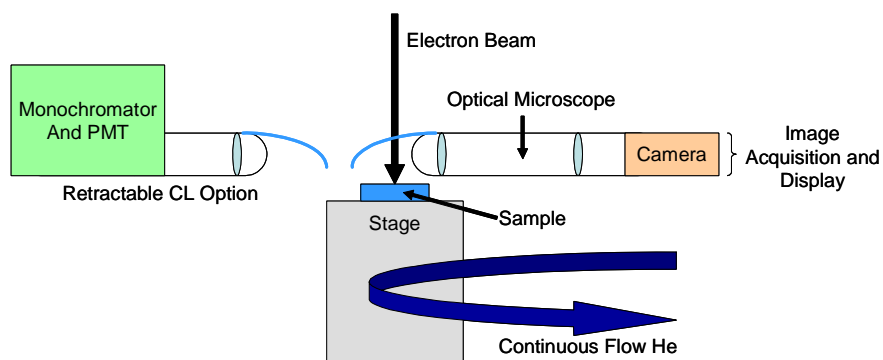


Figure 8. Schematic of Transport Imaging Components.

The operating modes of the SEM used in this work are the picture mode and spot mode. The picture mode is primarily used for helping with the focus of the optical microscope and allows for a picture of the area luminescence of the sample to compare with the spot mode. In picture mode, the SEM electron beam is rastered over the sample and the luminescence is imaged by the CCD. Figure 9 shows an image taken in SEM picture mode of n-doped p-type InGaP. The bright edge near the bottom with the large luminescence spot in the bottom right corner are the result of the SEM scanning one edge of the raster area longer than the rest of the area.

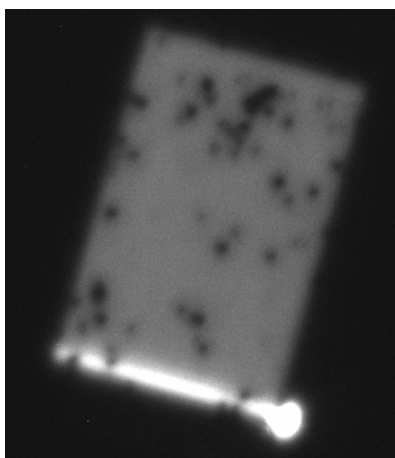


Figure 9. Image of n-doped InGaP in Picture Mode ( $140\ \mu\text{m} \times 160\ \mu\text{m}$ ).

The majority of the work done for diffusion length imaging is done in the spot operation mode. The diffusion length measurements that this work

ultimately extracts use this operating mode to create the images. The electron beam is held fixed on the sample and the distribution of the resultant luminescence across the sample shows the diffusion of the minority charge carriers. Figure 10 shows a spot mode image taken on a p-type doped GaAs sample.

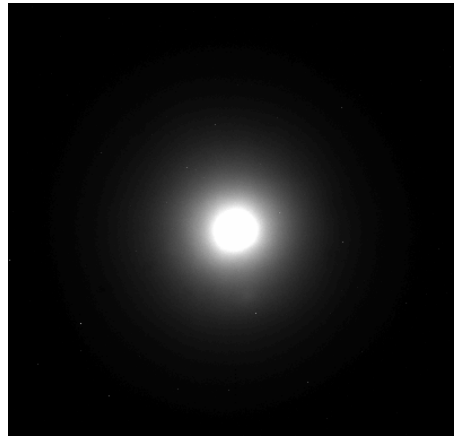


Figure 10. Image of doped p-type GaAs in Spot Mode ( $160\text{ }\mu\text{m} \times 160\text{ }\mu\text{m}$ ).

The bright, middle portion of the spot shown in Figure 9 is not the size of the electron beam that is hitting the sample, nor is it an image of the electron beam itself. The spot image is the actual sample luminescence created by the electron-hole recombination. The bright spot seen in the image is much bigger than the actual electron beam size on the sample surface for two reasons. First, the electron beam spreads out as it penetrates the sample. So, the size of the electron beam interaction region within the sample is more important. Secondly, the software used to display the image has a pixel dynamic range that can be modified. Changing the dynamic range allows all intensities above a certain level (the center of the spot) to be set as the high point of the dynamic range. This allows more insight into the regions further away from the center of the electron beam. If the dynamic range were not changed, only the very center of the spot would be bright, corresponding to the size of the electron beam within the sample. This is clear from Figure 11 which gives the horizontal line profile (intensity value as a function of position) of the spot image.

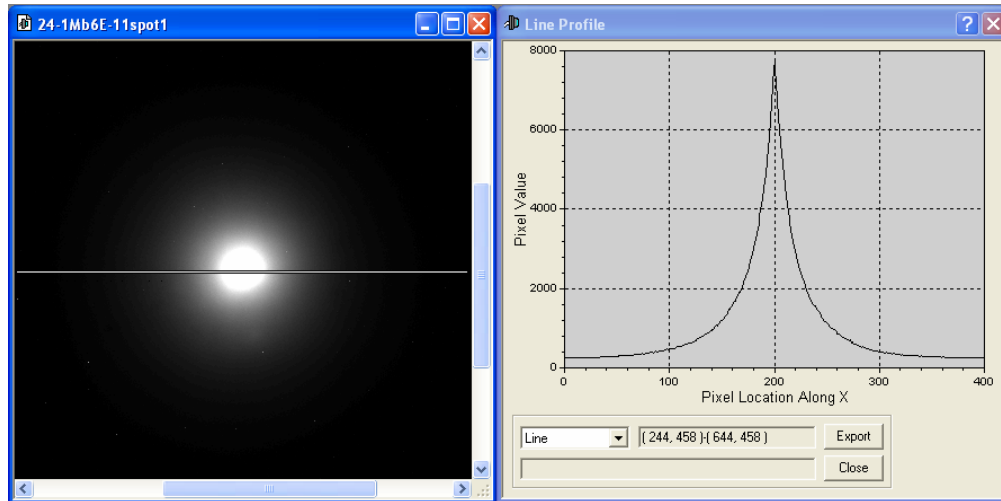


Figure 11. Image and Horizontal Line Profile of doped p-type GaAs.

From the line profile illustrated in Figure 11, the diffusion length can be extracted. Understanding how the electron beam interacts with a thin, two-dimensional structure and how the electrons diffuse within that 2-D structure is essential to extracting accurate diffusion length measurements. The next chapter explains the modeling and extraction technique used to obtain the diffusion length from the image and corresponding line profile.

THIS PAGE INTENTIONALLY LEFT BLANK

## IV. DIFFUSION LENGTH EXTRACTION STUDIES

### A. DIFFUSION LENGTH EXTRACTION METHODOLOGIES

In order to accurately extract the diffusion length from luminescence images for the various materials, it is imperative to understand the transport of the minority charge carriers within the sample. Therefore, a theoretical model for the diffusion of minority charge carriers from a fixed generation point is required. For a point source of generation, it has been shown that minority charge carrier concentration ( $\varpi(x, y)$ ) in 2 dimensions is given by:

$$\varpi(x, y) = \frac{g}{2\pi L^2} e^{\left(\frac{Sx}{2L^2}\right)} K_0 \left( \frac{\sqrt{S^2 + 4L^2}}{2L^2} r \right) \quad (8)$$

where  $S$  is the drift length ( $\mu\tau E$ ),  $L$  is the diffusion length,  $g$  is proportional to the generation rate,  $r = \sqrt{(x^2 + y^2)}$ , and  $K_0$  is the zeroth-order modified Bessel function of the second kind [8].

However, the electron beam is not an infinitesimally small point source, but rather a small, finite region on the sample where charge is generated. If a Gaussian form of the incident electron beam is used ( $m/\pi \exp[-m(x^2 + y^2)]$ ), then the resulting minority carrier distribution of charge would be:

$$\varpi(x, y) = \frac{gm}{2\pi^2 L^2} \int_{-\infty}^{\infty} \int_{-\infty}^{\infty} e^{-[m(\eta^2 + \xi^2)]} e^{\left(\frac{S(x-\eta)}{2L^2}\right)} K_0 \left( \frac{\sqrt{S^2 + 4L^2}}{2L^2} \sqrt{(x-\eta)^2 + (y-\xi)^2} \right) d\eta d\xi \quad (9)$$

where  $\eta$  and  $\xi$  are the integration variables in  $x$  and  $y$ ,  $m = 1/(2\sigma^2)$  is a beam size parameter where  $\sigma$  is the standard deviation, and all other parameters have been previously defined [9]. The experimental approach pursued in this work did not involve the use of applied electric fields. With no applied electric fields, the minority charge carriers do not drift, and therefore, the drift length  $S$  equals zero. With  $S = 0$ , Equation 9 reduces to the form:

$$\varpi(x, y) = \frac{gm}{2\pi^2 L^2} \int_{-\infty}^{\infty} \int_{-\infty}^{\infty} e^{-[m(\eta^2 + \xi^2)]} K_0 \left( \frac{1}{L} \sqrt{(x-\eta)^2 + (y-\xi)^2} \right) d\eta d\xi. \quad (10)$$

Although Equation 10 is the model for the minority charge carrier distribution with a charge generation point source, an approximate form would be easier to utilize to extract the diffusion length. It has been shown that in the limit of large distances from the center, the Bessel function  $K_0$  can be approximated by a decaying exponential function, regardless of the details of the center region, including the Gaussian electron beam generation area [10]. Therefore, the distribution, and hence the photon intensity from electron-hole recombination can be approximated as:

$$I \sim I_0 e^{-C \cdot x}, \text{ where } C = \frac{1}{L} \quad (11)$$

in the limit  $x \gg L$ . Equation 11 allows for the extraction of the diffusion length simply by calculating the slope of a semi-logarithmic plot of intensity versus position. This technique is designated as the 1/Slope Technique and is described in the next section.

## 1. 1/Slope Technique

As described by Equation 11, the diffusion length of minority carriers in a sample externally excited at a quasi-point source can be extracted by calculating the slope of a semi-logarithmic plot of intensity versus position. However, this approximation is based on the limit of the Bessel function far away from the center of the generation point. The question is, how far away from the center and the charge generation point is far enough? To answer that question, the minority carrier charge distribution described by Equation 10 was modeled in Mathcad with no applied electric field for a range of diffusion lengths. The results of the model were placed into SigmaPlot, a technical graphing and data analysis software package, for analysis. The results were first normalized, and graphed, showing the expected distribution of the minority charge carriers for different

diffusion lengths. Figure 12 shows these modeled distributions of normalized intensity versus position in microns for multiple diffusion lengths (in microns) and a Gaussian electron beam size of 1.5 microns ( $m = 3.5$ ).

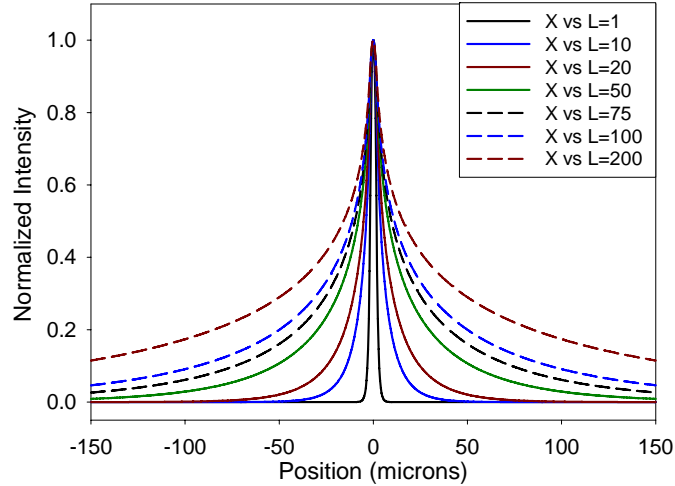


Figure 12. Modeled Distribution of Minority Charge Carriers (After: [11]).

With the expected distribution of the minority charge carriers, the data can be graphed on a semi-logarithmic graph, and the slope of that distribution is the reciprocal of the estimated diffusion length. These diffusion lengths, and the distance out from the center of the spot are compared to the actual diffusion lengths. Figure 13 shows the relationship between two ratios, the inverse slope to the actual diffusion length and the distance from the center of the generation point where the slope value was extracted to the actual diffusion length.

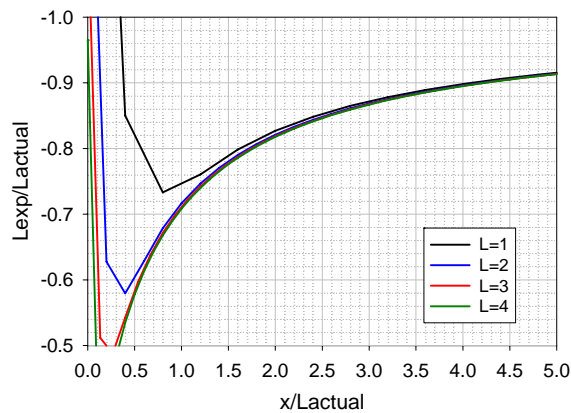


Figure 13. Error of Estimated Diffusion Length as a Function of Distance from Charge Generation Center (After: [11]).

The significance of Figure 13 is that the percent error of the estimated diffusion length to the actual diffusion length can be estimated via the distance from the charge generation center to where the slope value was obtained. For instance, the figure shows that if the slope is obtained at a distance of 9 times the actual diffusion length from the charge generation center, the estimated diffusion length will be 95% of the actual value, or have only a five percent error [11]. However, if the slope is taken closer to the center, at only five times or two times the actual diffusion length, the estimated diffusion length will underestimate the value by 10% or 20%.

A p-type GaAs sample doped at a level of  $9.7 \times 10^{15} \text{ cm}^{-3}$  is used as an example and illustrates the 1/Slope technique of extracting diffusion length. The double heterostructure GaAs layer has a thickness of 1.9 microns and a minority carrier effective lifetime of 20.3 nanoseconds, determined from time-resolved photoluminescence. Figure 14 shows an image of the diffusion of the minority charge carriers under spot excitation from the SEM at a probe current of  $6 \times 10^{-11} \text{ A}$  and electron beam energy of 20 keV, for an exposure time of 25 sec.

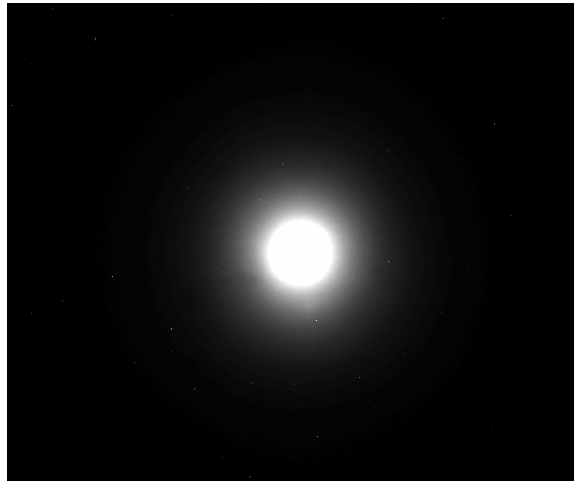


Figure 14. Image of Luminescence Distribution in GaAs ( $245 \mu\text{m} \times 210 \mu\text{m}$ ).



From the image, a horizontal line profile is taken and imported into SigmaPlot, the graphing and data analysis software used in this work. The data are then normalized and the noise floor of the CCD camera is subtracted via the equation:

$$I_{Norm} = \frac{I - I_{Noise}}{I_{Max} - I_{Noise}}. \quad (12)$$

The normalized intensity plotted as a function of position yields the result in Figure 15. A semi-logarithmic plot of the data from Figure 15 is shown in Figure 16.

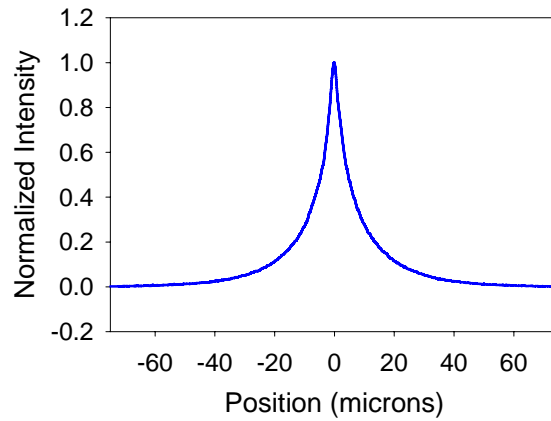


Figure 15. Normalized Intensity as a Function of Position.

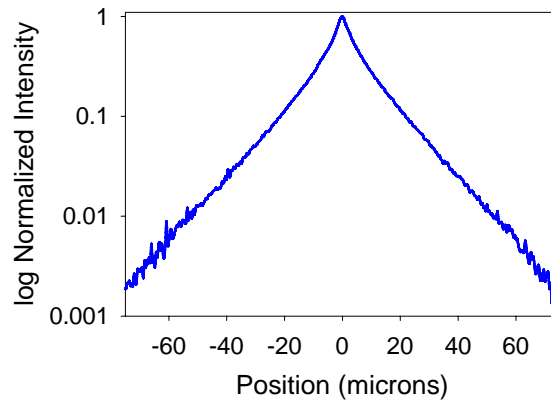


Figure 16. Semi-logarithmic Plot of Normalized Intensity as a Function of Position.

The plot of the semi-logarithmic plot of normalized intensity versus the position from the center of the charge generation as shown in Figure 16 is used to choose how far away from the charge generation center to take the slope value. As stated earlier, taking the slope value farther away from the spot center will yield estimated diffusion lengths with smaller errors. However, the farther away from the charge center, the noisier the experimental data get. For the example to illustrate the 1/Slope technique, the slope value was extracted at  $35 \pm 15$  microns from the charge generation center. Figure 17 shows the data from both the left and right sides of the distribution and the linear regression lines extracted from the data.

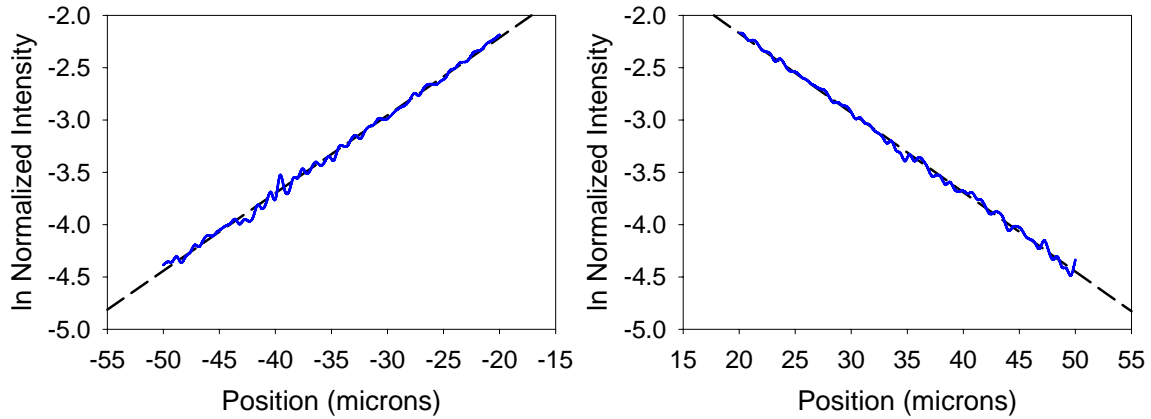


Figure 17. Semi-logarithmic Plot of Normalized Intensity as a Function of Position and Linear Regression Lines for Slope extraction.

From the linear regression lines in Figure 17, a SigmaPlot subroutine extracts the slope value, the standard error, and the  $R^2$  value. The slope value is used to estimate the diffusion length, and the standard error is used to estimate the error bars on the calculated value. The  $R^2$  value is used as a figure of merit of how well the data fit the linear regression. Table 1 shows the results of the linear regression, the estimated diffusion lengths extracted, and the mobility of the minority charge carriers based on the lifetime numbers obtained via TRPL, for the luminescence profiles to the right and left of the charge generation point.

As stated earlier, however, these estimated slope values have errors associated with them, due to the fact that the slope was extracted at a point that is not completely in the decaying exponential limit of the Bessel function. For this example, the position of the extracted slope is  $35\ \mu\text{m}$ , and the estimated diffusion length is  $13.5\ \mu\text{m}$ . If we use the estimated diffusion length as the actual diffusion length, the slope value is extracted 2.6 times the diffusion length away from the charge generation center. Referring back to Figure 13, a slope value extracted only 2.6 times away from the center will lead to the estimated diffusion length 85% of the actual diffusion length. Therefore,  $15.9\ \mu\text{m}$  is a better estimate for the actual diffusion length. With this value, the slope value is extracted 2.2 times the diffusion length away from the center, which corresponds to the estimated diffusion length being 82.5% of the actual diffusion length. This yields a  $16.4\ \mu\text{m}$  estimate for the actual diffusion length. Further iterations can take place, but increased errors can be introduced due to inaccuracies in reading the graph in Figure 13. Extracting the diffusion length via this method is called using the T-factor [11]. The results labeled  $L_{\text{DIFF}}$  (T-factor) in Table 1 give the values of the diffusion lengths extracted from the estimated 1/Slope diffusion lengths via the process described above and utilizing the T-factor correction from Figure 13. Corresponding mobility values are calculated based on independent lifetime (TRPL) measurements.

SAMPLE	LIFETIME	SLOPE	StdErr	$L_{\text{DIFF}}$ (1/slope)	+/-	$\mu$	$R^2$	$L_{\text{DIFF}}$ (T-factor)	$\mu$
	ns	$\mu\text{m}^{-1}$	$\mu\text{m}^{-1}$	$\mu\text{m}$	$\mu\text{m}$	$\text{cm}^2/\text{Vs}$		$\mu\text{m}$	$\text{cm}^2/\text{Vs}$
GaInAs (0% In) (GaAs)	20.3	0.07432	0.00049	13.5	0.1	3530	0.997	16.4	5250
GaInAs (0% In) (GaAs)	20.3	0.07596	0.00045	13.2	0.1	3380	0.997	15.9	4930

Table 1. Results of 1/Slope Technique on GaAs Sample.

Although this technique yields a reasonably accurate diffusion length, other techniques of extracting diffusion length were investigated. One of the limitations of this technique is that the slope must be far away from the charge generation center. However, if the slope is known at a certain distance away from the charge generation center, a more accurate measure of diffusion length would be to model the charge distribution at different diffusion lengths and

compare the model slope at the same distance away from the charge generation center. The next section details this technique for diffusion length extraction, which is called the Slope Matching technique.

## 2. Diffusion Length Look-up via Model Slope Matching

The Slope Matching technique compares model simulations of different diffusion lengths to the experimental data. The position where the slope value is extracted is known and is compared to simulation slope values at the same position. The simulation slope value that matches the experimental slope value the closest will indicate the diffusion length. To illustrate and explain this technique, the GaAs sample and experimental data used to illustrate the 1/Slope technique will be utilized again.

The slope of the GaAs luminescence distribution, as shown in Figure 17, is compared with the slope graphs of simulations with diffusion lengths varying from 13-17 microns. Figure 18 shows this comparison and illustrates that the slope of the experimental data can not be matched to the corresponding modeled slope line with this information alone.

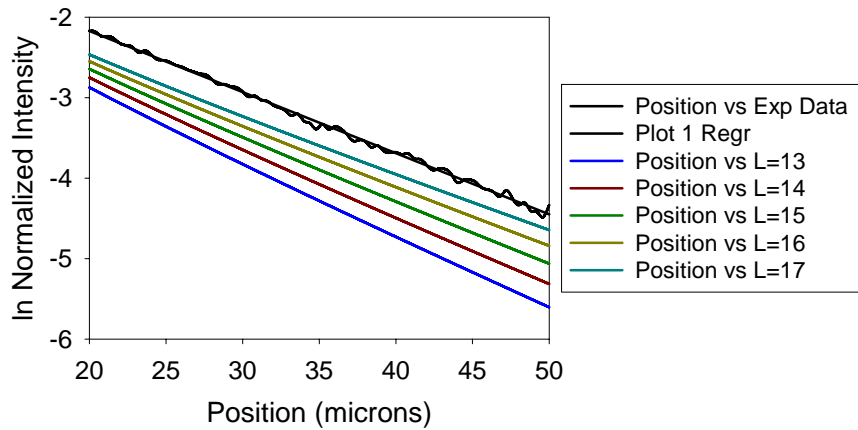


Figure 18. Experimental and Modeled Slope Data Comparison.

For a more accurate slope match, the slopes of the modeled data are extracted from a range of diffusion lengths from 2-20 microns. The slopes are then plotted versus their corresponding diffusion length, and a simple spline curve is used to connect all the data points. Figure 19 shows this data on the left

and is used to extract the diffusion length of the experimental data based upon the slope of the experimental data. The right graph in Figure 19 is expanded near the slope values listed in Tables 1 & 2, along with the standard error associated with the slopes. The graph shows the extraction of the diffusion length and associated error from the slope and slope error values. The results are shown in Table 2. These slope matching values closely match the T-factor diffusion lengths computed in Table 1.

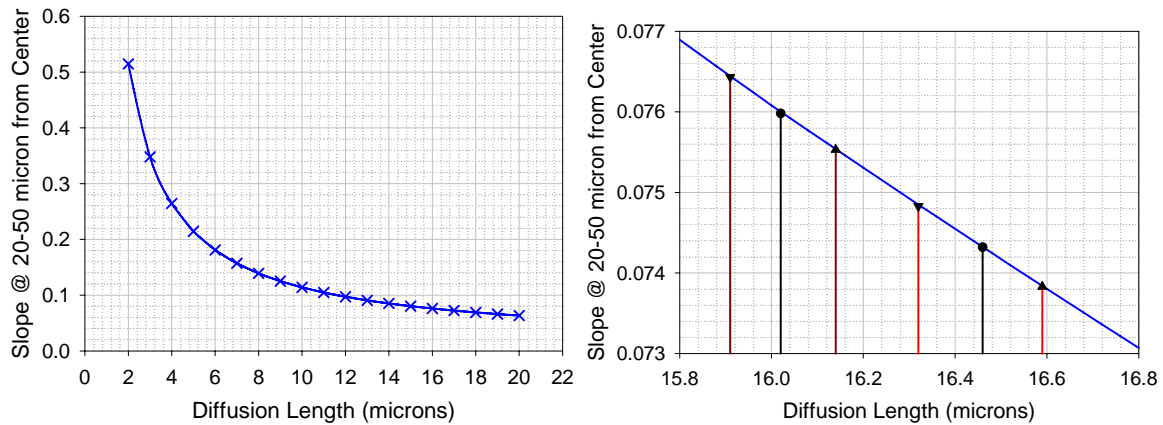


Figure 19. Modeled Slope values versus Diffusion Length and Diffusion Length Extraction from Experimental Data.

SAMPLE	LIFETIME	SLOPE	StdErr	$L_{DIFF}$ (1/slope)	+/-	$\mu$	$R^2$	$L_{DIFF}$ (slope match)	+/-	$\mu$
	ns	$\mu m^{-1}$	$\mu m^{-1}$	$\mu m$	$\mu m$	$cm^2/Vs$		$\mu m$	$\mu m$	$cm^2/Vs$
GaInAs (0% In) (GaAs)	20.3	0.07432	0.00049	13.5	0.1	3530	0.997	16.5	0.14	5280
GaInAs (0% In) (GaAs)	20.3	0.07596	0.00045	13.2	0.1	3380	0.997	16.0	0.12	5010

Table 2. Results of Slope Matching Technique on GaAs Sample.

The slope matching technique does give good results; however, it is time consuming to obtain the results. The slope charts must be reproduced for each individual extraction, unless the slope extracted from the experimental data is within the same exact range of a model run already accomplished. Since the slope should be taken as far away from the center as possible, limiting analysis to previous model runs can result in taking the slope value at an undesirable distance from the center spot.

The slope matching technique does lend itself to more in-depth analysis of the electron beam/sample interaction. A two-parameter fit of the model data to the experimental data extracts both the diffusion length and the electron beam interaction dimension within the sample itself. It has been shown that the electron beam on the JEOL 840A SEM at a probe current of  $1 \times 10^{-10}$  A and an accelerating voltage of 30 keV yields an incident beam diameter of 96 nm [12]. This is the size of the beam on the surface of the sample. The electron beam interacts with atoms as it enters the sample, and these interactions (elastic scattering) deflect the electrons within the beam along new trajectories, causing them to spread out laterally from the incident beam footprint [13]. This spreading of the beam within the sample is modeled by the parameter  $m$ , which for a Gaussian distribution,  $m = (1/2\sigma^2)$ , where  $\sigma$  is the standard deviation of the distribution. For a Gaussian distribution, 95% of the distribution is contained within  $2\sigma$  of the center.

Using Equation 9 or 10 to model the distribution, multiple model runs were executed to find the best two-parameter fit for the GaAs sample. The best fit of the model to the experimental results show that the best two-parameter fit is a diffusion length of  $16 \mu m$  and a  $m$  value of 0.5. The  $m$  value results in a standard deviation of the charge generation distribution within the sample of  $1 \mu m$ , with 95% of the electrons within  $2 \mu m$  of the generation center. Figure 20 shows the best-fit model along with the experimental data. It is interesting to note that the size of the electron beam within the sample has little effect on the slope values away from the charge generation center, and therefore, little effect on the extracted diffusion length. As long as the slope values are taken  $2\sigma$  away from the beam center, variations of the slope values are negligibly affected by the beam size parameter.

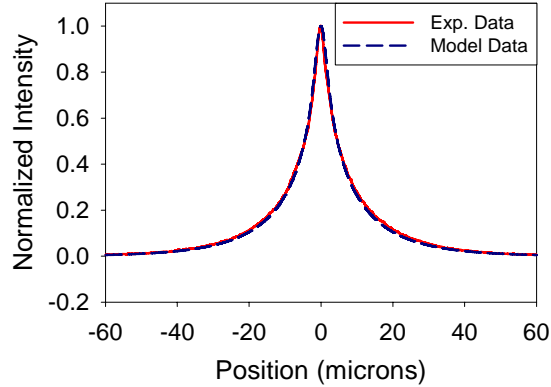


Figure 20. Two-Parameter Fit of Model to Experimental Data on GaAs Sample.

## B. TRIPLE JUNCTION SOLAR CELL MATERIALS

Using the two techniques to extract diffusion length previously described, an in-depth analysis of materials characterized in this work is now presented. The samples are all double heterostructures of the p-type layers within a triple junction solar cell. As stated earlier, a typical triple junction solar cell, such as the Spectrolab UTJ, is an InGaP/InGaAs/Ge cell, with the top cell being InGaP, the middle cell InGaAs, and the bottom cell Ge [3]. Both the InGaP layers and the InGaAs layers were analyzed. No characterization was performed on the Ge layer.

The double heterostructure configuration of the samples is illustrated in Figure 21 with a simple schematic. Additionally, the band diagram of the double heterostructure is also shown in Figure 21. The double heterostructure of the samples is important for transport imaging for two reasons. The thin double heterostructure can be treated as a two dimensional structure, and the two barrier layers eliminates surface recombination of the charge carriers. By removing the potential influence of surface recombination, the measured diffusion lengths are more fundamentally representative of the layer material.

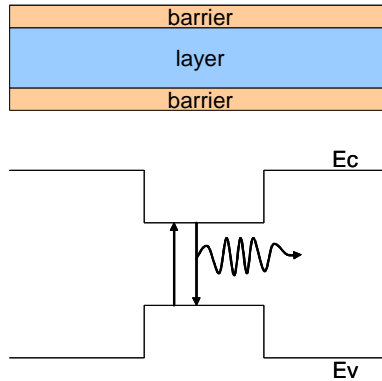


Figure 21. Schematic and Band Diagram of Double Heterostructure.

### 1. Indium Gallium Phosphide Double Heterostructures

The Indium Gallium Phosphide layer is the top cell in a triple junction solar cell. It has the largest band-gap of all the cells and therefore absorbs the higher energy photons compared to the rest of the cell [Refer back to Figure 1 to see the absorption spectrum of InGaP]. The InGaP layer is arguably the most important layer in the triple junction solar cell. As shown in Figure 3, the triple junction cell is three separate cells stacked in series. In series, the cell that produces the least amount of current limits all the cells in series to that current value. Figure 22 shows the current vs. voltage (I-V) characteristic curves for Ge, Si, GaAs, and InGaP solar cells under AM0 solar illumination. The figure clearly shows that the InGaP cell, while having the largest open circuit voltage, also has the most limiting short circuit current. Therefore, in triple junction solar cells, the InGaP layer is the limiting layer in regard to current flow throughout the cell.



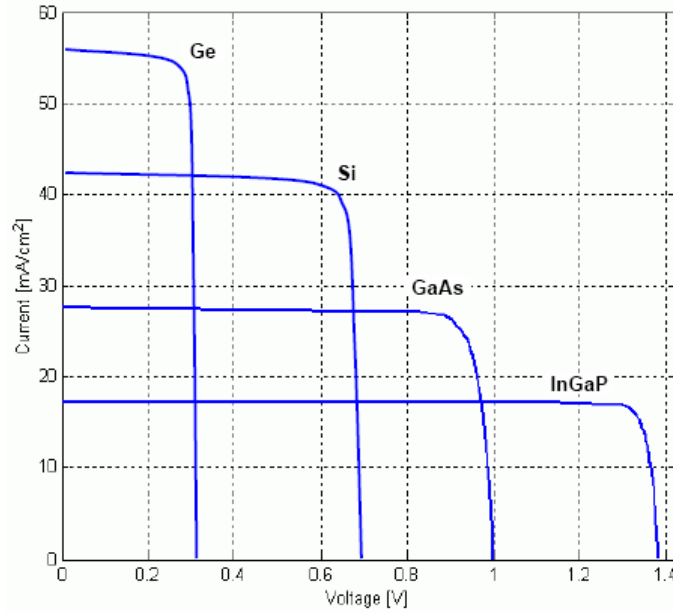


Figure 22. I-V Curves for Ge, Si, GaAs, and InGaP Cells Under AM0 Solar Illumination (From: [4]).

InGaP solar cells have another characteristic that involves the ordering or disordering of the indium and gallium atoms. Lattice matched InGaP is comprised of 49.6% indium and 50.4% gallium, commonly denoted as  $\text{In}_{.496}\text{Ga}_{.504}\text{P}$ . The ordering of InGaP is due to the atomic arrangement of the Group III elements (In and Ga) on the Group III sub-lattice [14]. This is more clearly illustrated in Figure 23, which shows the zinc blende (ZnS) cubic crystal structure, which is the crystal structure of InGaP. The atoms labeled S in Figure 23 are the Ga/In atoms, while the Zn labeled atoms are the P atoms in InGaP. The ordering of the Ga/In plane within the crystalline structure is characterized by CuPt ordering, one of the most widely studied types of long range ordering with alternating planes occupied by atoms from the Group III elements. Figure 24 shows simulations of the ordering and disordering of Group III or V sub-lattice for electron diffraction patterns done by Dobročka, Vávra and Wallenberg [15] that show ordered and disordered domains of the CuPt-type ordering in the Ga/In plane.

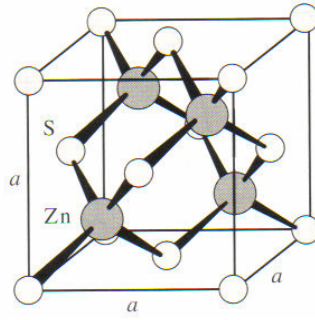


Figure 23. Zinc Blende Cubic Crystal Structure (From: [1]).

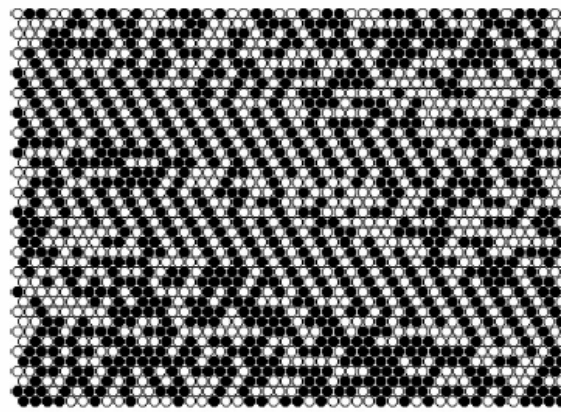


Figure 24. Ordered and Disorder Domains of CuPt ordering in III-V Semiconductor Alloys (From: [15]).

The importance of the ordering of the Ga/In planes of InGaP is that the band-gap of InGaP is dependent on the ordering [14]. This allows for additional tuning of the band-gap within the InGaP layer of a triple-junction solar cell. Higher efficiencies of output power can be obtained with a larger band-gap, since the tuning of the band-gap increases the open circuit voltage while not changing the short circuit current. Additionally, radiation-induced sub-lattice order-disorder transition shows the defects produced within InGaP by radiation have a smaller effect on carrier recombination dynamics than radiation induced defects in GaAs [16]. This result is significant in producing radiation tolerant solar cells for space applications.

Finally, one avenue of research in more efficient solar cells is growing non-lattice matched solar cells. Most triple junction cells today are lattice matched (LM) to the cell base, which is Ge. InGaP grown to the specification of 49.6% In and 50.4% Ga is LM to Ge. Lattice matching to the base material ensures that no edge dislocations are formed in between the two layers. These dislocations decrease efficiency of charge transport across the two layers. However, the band-gap of the InGaP semiconductor grown by metalorganic chemical vapor deposition will vary depending on the ratio of the In and Ga in the gas phase [14]. This also allows for the tuning of the band-gap, although the main push of this non-lattice matched, or metamorphic (MM), research is to tune the InGaAs band-gap. This will be explained in the next section. Figure 25 shows that the luminescence spectrum of doped MM InGaP is shifted to longer wavelengths when compared to nid LM InGaP.

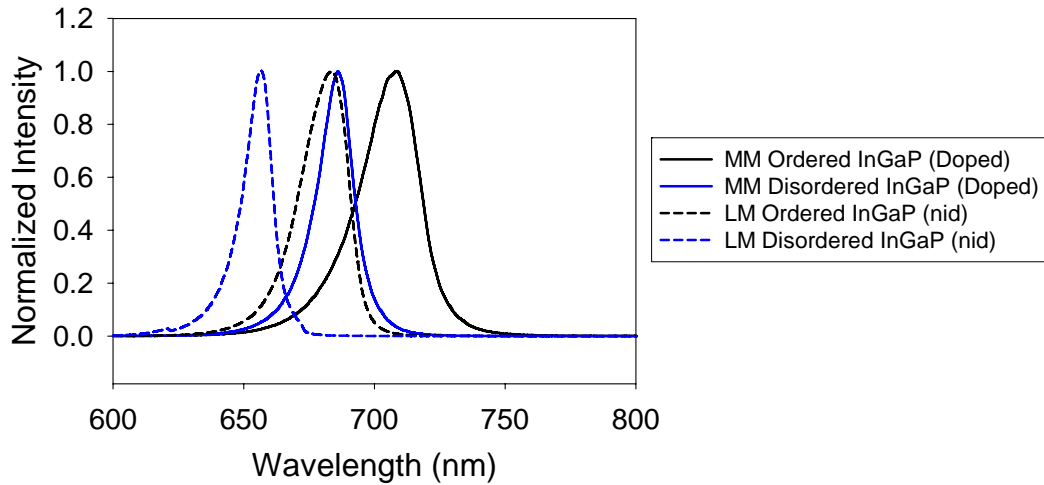


Figure 25. CL Spectra of doped MM and nid LM InGaP.

Table 3 summarizes the material parameters for all the InGaP double heterostructures that were analyzed in this work. The table shows that a mix of LM to MM and ordered to disordered samples were analyzed, at various doping levels. All the MM samples are lattice matched to 8%-In InGaAs. The results of the analysis are presented in the Experimental Results section of this thesis.

SAMPLE	SAMP #	LM or MM	Ordering	Layer Thickness $\mu\text{m}$	DOPING $\text{cm}^{-3}$	LIFETIME ns
InGaP (49.6% In)	24-1Tb	LM	Ordered	0.65	$1.10\text{E}+17$	13.1
InGaP (49.6% In)	23-1Tb	LM	Ordered	0.70	$1.53\text{E}+17$	15.4
InGaP (56.2% In)	25-6Tb	MM	Ordered	0.50	$2.83\text{E}+17$	1.4
InGaP (49.6% In)	24-3Tb	LM	Disordered	0.75	$2.70\text{E}+17$	10.2
InGaP (56.2% In)	25-3Tb	MM	Disordered	0.55	$3.83\text{E}+17$	4.5
InGaP (49.6% In)	564-1Tb	LM	Ordered	0.80	nid	46.5
InGaP (49.6% In)	564-BTb	LM	Disordered	0.80	nid	21.5

Table 3. InGaP Double Heterostructures Sample Parameters.

## 2. Indium Gallium Arsenide Double Heterostructures

The Indium Gallium Arsenide layer is the middle cell in a triple junction solar cell. It has a band-gap smaller than InGaP, but larger than Ge, allowing it to absorb photons not absorbed by InGaP, but allowing lower energy photons through to the Ge cell [Refer back to Figure 1 to see the absorption spectrum of GaAs (0%-In InGaAs)]. As shown in Figure 22, the I-V characteristic curve for GaAs has a larger short circuit current, but a smaller open circuit voltage. As explained earlier, the InGaP layer limits the current in the InGaAs layer due to the cells being stacked in series. However, the open circuit voltage across the entire triple junction solar cell is the sum of all the open circuit voltages of the individual cells. Therefore, in triple junction solar cells, there is no single layer that limits the overall voltage across the cell.

As with InGaP, lattice matching is important for efficient operation of the solar cell. InGaAs with 1%-In and 99%-Ga is lattice matched to the Ge base, and this mixture ratio is commonly denoted as  $\text{In}_{.01}\text{Ga}_{.99}\text{As}$ . Again, lattice matching to the base material ensures that minimal edge dislocations are formed in between the two layers, keeping efficiency high. However, just like InGaP, the varying of the ratio between In and Ga can change the band-gap of the material. For example, 8%-In InGaAs has a band-gap of approximately 1.3 eV, while 1%-In InGaAs has a band-gap of approximately 1.4 eV. The thrust of the research to incorporate MM InGaAs in solar cells with a Ge base is to manufacture 4- or 5-junction solar cells that break up the solar spectrum among even more layers than illustrated in Figure 1. Figure 26 shows the luminescence spectrum of doped GaAs and LM InGaAs.

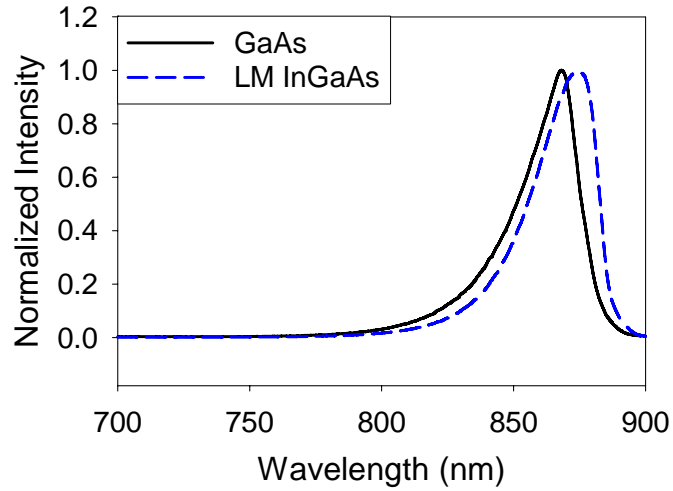


Figure 26. CL Spectra of GaAs and 1%-In InGaAs.

Table 4 summarizes all the InGaAs double heterostructures that were analyzed in this work. The table shows that a mix of LM to MM samples was analyzed, at various doping levels. All the MM samples are 8%-In InGaAs and are lattice mismatched to the Ge base. The results of the analysis are presented in the Experimental Results section of this thesis.

SAMPLE	SAMP #	LM or MM	Layer Thickness $\mu\text{m}$	DOPING $\text{cm}^{-3}$	LIFETIME ns
InGaAs (0% In)	24-1Mb	--	1.90	9.67E+15	20.3
InGaAs (1% In)	23-1Mb	LM	1.90	1.07E+16	433.0
InGaAs (8% In)	25-6Mb	MM	2.00	1.70E+16	5.8
InGaAs (0% In)	24-3Mb	--	1.70	1.67E+16	12.1
InGaAs (8% In)	25-3Mb	MM	2.20	1.73E+16	9.3
InGaAs (8% In)	565-BMb	MM	3.44	nid	10.4

Table 4. InGaAs Double Heterostructures Sample Parameters.

### 3. Experimental Results

Although Lubber et. al. [9] developed the technique to image the drift and diffusion of minority charge carriers in a modulation doped p-type GaAs heterostructure, the ability to image diffusion in a wider range of materials, with widely varying diffusion lengths, was unproven. The first unequivocal evidence of imaging diffusion of the minority charge carriers for a range of materials is shown in Figure 27. This series of images shows the distribution of electron-hole

recombination luminescence from four different samples, each excited by an electron beam in spot mode with the same beam energy (20 keV) and probe current ( $6 \times 10^{-11}$  A). Additionally, all these samples were in the SEM at the same time, and the SEM beam was on continuously throughout the data collection process. This eliminates any potential variation due to SEM filament differences or alignment.

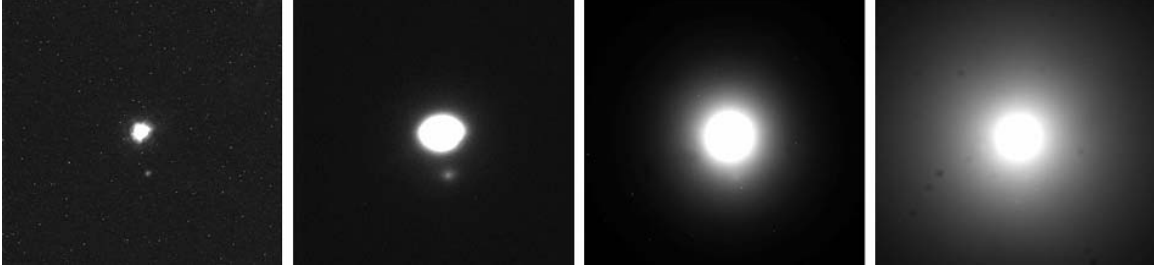


Figure 27. Distribution of Luminescence of Samples 564-1Tb, 24-1Tb, 24-1Mb and 23-1Mb under SEM Spot Mode Excitation (all pictures  $160 \mu\text{m} \times 160 \mu\text{m}$ ).

Using the techniques described in Section A of this chapter, one dimensional line profiles were extracted from these images, the noise-floor subtracted off and the luminescence profiles were normalized. Diffusion lengths were obtained either with the 1/slope method or slope matching technique. The modeled data compared to the experimental data are shown in Figure 28. The figure illustrates that the experimental data follow the predicted behavior ( $\sim K_0(r/L_{\text{Diff}})$ ) for diffusion in 2d from a Gaussian spot generation.

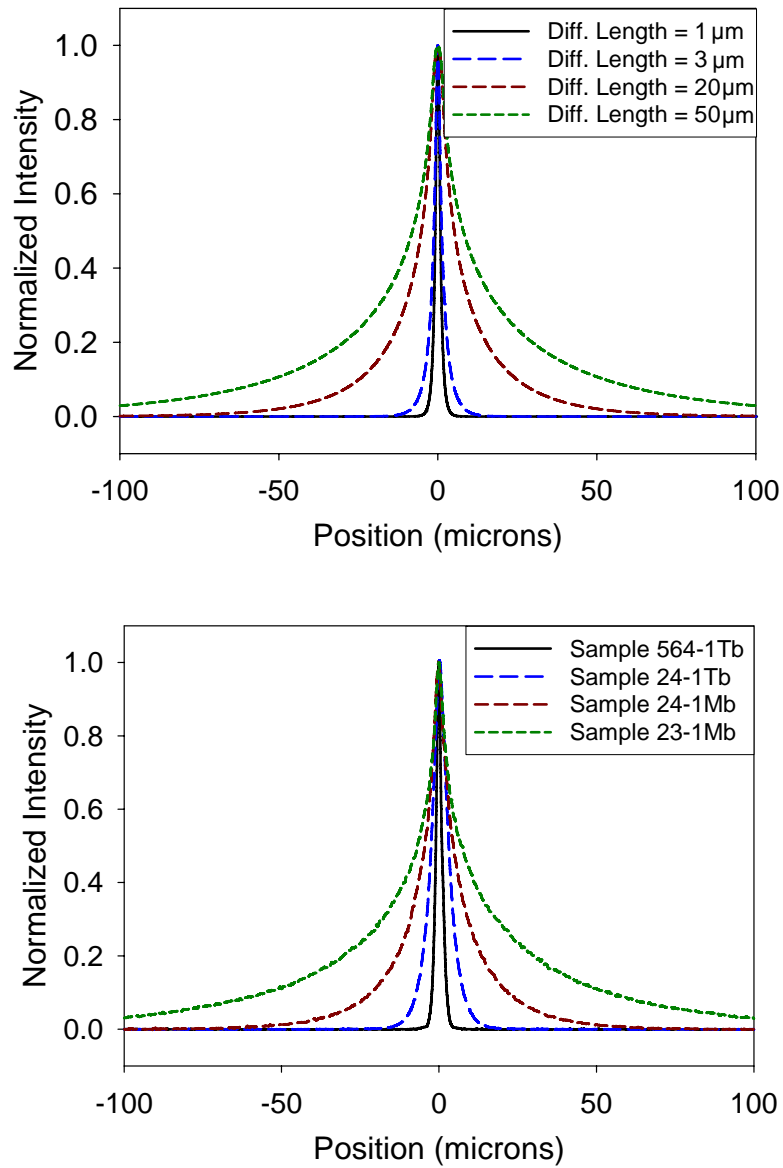


Figure 28. Modeled and Experimental Data of 564-1Tb, 24-1Tb, 24-1Mb and 23-1Mb.

The results of the analysis on all the samples are summarized in Table 5. This table gives the diffusion lengths for the samples from the 1/Slope method, the T-factor method and the Slope matching look-up process.

SAMPLE	SAMP #	DOPING	LIFETIME	$L_{DIFF}$ (1/slope)	$\mu$	$L_{DIFF}$ (look-up)	$\mu$	$L_{DIFF}$ (T-factor)	$\mu$
		$cm^{-3}$	ns	$\mu m$	$cm^2/Vs$	$\mu m$	$cm^2/Vs$	$\mu m$	$cm^2/Vs$
InGaP LM Ordered	24-1Tb	1.10E+17	13.1	2.6	202	3.0	278	3.0	269
InGaP LM Ordered	23-1Tb	1.50E+17	15.4	3.5	310	4.2	448	4.1	431
InGaP MM Ordered	25-6Tb	2.83E+17	1.4	1.5	624	1.7	849	1.7	797
InGaP LM Disordered	24-3Tb	2.70E+17	10.2	3.2	410	4.0	614	3.9	583
InGaP MM Disordered	25-3Tb	3.83E+17	4.5	1.5	204	1.8	283	1.7	261
GaAs	24-1Mb	9.67E+15	20.3	13.6	3620	17.2	5770	16.2	5140
InGaAs LM	23-1Mb	1.07E+16	433.0	48.9	2180	61.9	3500	60.0	3290
InGaAs MM	25-6Mb	1.70E+16	5.8	4.4	1300	5.3	1940	5.0	1700
GaAs	24-3Mb	1.67E+16	12.1	15.6	7970	19.3	12200	18.9	11700
InGaAs MM	25-3Mb	1.73E+16	9.3	7.4	2340	9.0	3470	8.9	3360
InGaP LM Ordered	564-1Tb	nid	46.5	2.0	34	2.2	42	2.3	43
InGaP LM Disordered	564-BTb	nid	21.5	0.9	14	1.2	26	1.0	18
InGaAs MM	565-BMb	nid	10.4	1.2	57	1.7	106	1.4	76

Table 5. Diffusion Length Measurement Results for all Samples.

The results from the InGaP samples show that the diffusion lengths are sufficient enough to sustain the electrons in the conduction band for them to exit the cell. The typical width of the p-type region of the InGaP cell is 0.5-0.8  $\mu m$ , and the diffusion lengths of all the doped InGaP samples are greater than the thickness of the p-type region. An area of possible concern is the MM InGaP samples. Although the measured diffusion lengths of the MM samples were 1.7  $\mu m$  by the T-factor method, this approaches the lower limit of diffusion length this technique can measure due to limited sensitivity when the diffusion length is comparable to the generation region. We believe that the smallest diffusion length we can measure is  $\sim 1 \mu m$ , but further studies on the lower limit of the technique's capability need to be performed.

It is interesting to note that the diffusion length of the doped, disordered InGaP samples is comparable to the doped, ordered InGaP samples. Assuming the lower lifetime value is correct, the disordered InGaP must have a higher mobility value than ordered InGaP. This has been shown in literature to be true for n-type InGaP, where the electrons are the majority charge carriers [17]. However, this diffusion length variation of disordered to ordered may also be a result of the disordered sample have a higher doping value. Further studies involving multiple samples at different doping levels will answer those questions.



The InGaAs results suggest that the average lifetime numbers reported from TRPL may not be accurate. The two GaAs samples have comparable diffusion lengths, but their reported lifetimes are substantially different. Combining the diffusion length and the lifetime values, the calculated mobility values are vastly different. The sample 24-1Mb has a calculated mobility of  $5,100 \text{ cm}^2 / (\text{Vs})$ , while the sample 24-3Mb has a calculated mobility of  $11,600 \text{ cm}^2 / (\text{Vs})$ . Literature shows that the largest value of electron mobility as a majority charge carrier is approximately  $8,000 \text{ cm}^2 / (\text{Vs})$  [18]. Additionally, electron mobility as a minority charge carrier has been measured to be less than the electron mobility as a majority charge carrier [19]. The repeatability of our diffusion length measurements suggests that the lifetime numbers from TRPL require confirmation. This result shows that our technique can be used to check the results of the lifetime numbers extracted via TRPL, by simply checking to see if the mobility numbers yield realistic results.

As with the InGaP samples, it is desirable to show how the mobility changes as a function of the doping levels. However, a larger sample set is required to adequately assess the diffusion length and mobility changes as a function of doping. Also, the spatial variation and reproducibility of the lifetimes values needs to be better established before adequate comparisons can take place.

With the results above, the next section will focus on conclusions that can be drawn. Additionally, areas for future research are discussed and preliminary results of these future research areas are presented.

THIS PAGE INTENTIONALLY LEFT BLANK

## V. CONCLUSION AND SUGGESTION FOR FURTHER RESEARCH

### A. SUMMARY AND CONCLUSION

A quantitative and non-destructive method for extracting minority carrier diffusion lengths has been developed and demonstrated for doped heterostructures, specifically the p-type InGaP and InGaAs layers of a triple junction solar cell. This method advances the transport imaging technique and extracts the diffusion length from a single spot image taken with a SEM with an optical microscope. Diffusion lengths of  $1.2 - 4.2 \mu m$  were measured from doped and not intentionally doped p-type InGaP, illustrating that the diffusion length is greater than the layer thickness. Diffusion lengths of  $1.7 - 61.9 \mu m$  were measured for GaAs, LM InGaAs and MM InGaAs, and the results showed that the diffusion lengths in the doped samples are greater than the layer thickness. This work, comparing multiple samples under the same excitation conditions, clearly demonstrates the dependence of luminescence distribution on material parameters.

The diffusion length results, when combined with minority carrier lifetime values from TRPL, show that calculated mobility numbers are not always in consistent with past experimental results. With the demonstrated repeatability shown in the diffusion length measurements, the repeatability and accuracy of the lifetime values from TRPL appears to be a limitation in the determination of mobility values. This was most clearly shown with the two GaAs sample. One sample had a calculated mobility of  $5,100 cm^2/(Vs)$ , well within the expected range of  $4,000-8,000 cm^2/(Vs)$  [18]. The other sample had a calculated mobility of  $11,600 cm^2/(Vs)$ , which is well outside of the expected value.

In conclusion, the imaging transport technique has advanced to extract diffusion length values with a single, non-destructive and contact-free measurement. This technique can be used with current and potential solar cell materials to measure key parameters to ensure efficient operation of the solar

cell, as demonstrated with the InGaP and InGaAs layers in a current triple junction solar cell and to provide timely, relevant characterization for new material development.

## **B. SUGGESTIONS FOR FURTHER RESEARCH**

### **1. Crystallographic Directionality Dependence of Diffusion Length**

Through the development of the imaging transport technique on solar cell layers, many different materials with alloy compositions and doping levels were analyzed multiple times. After multiple measurements were taken, the measurements were compared to ensure repeatability was obtained. One such sample was 24-1Tb, a doped, lattice-matched ordered InGaP double heterostructure sample. In this case, the sample was placed in the SEM on 28 September 2006 and a measurement was taken. The sample was then removed from the SEM while other measurements were taken. On 3 October 2006, the same sample was placed back in the SEM, but this time rotated approximately 90° from the previous orientation. Figure 29 shows the images taken by the CCD camera of the InGaP sample 24-1Tb, both with an electron beam energy of 20 keV, probe current of  $6 \times 10^{-11}$  A and an exposure time of two seconds.

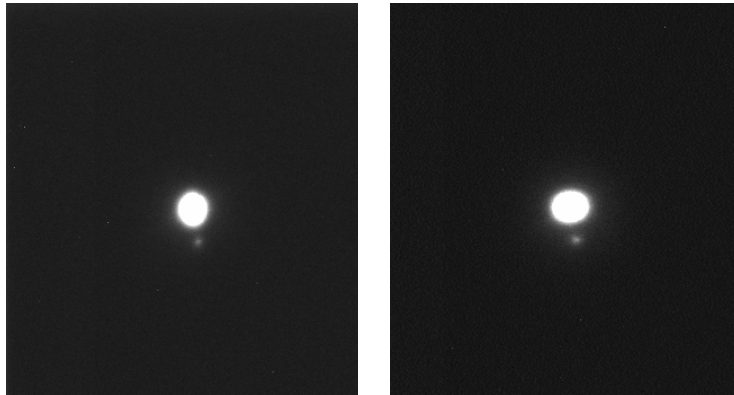


Figure 29. Images ( $250 \mu\text{m} \times 275 \mu\text{m}$ ) of Sample 24-1Tb taken on 28 September and 3 October Respectively.

Figure 29 clearly shows that there is a directional anisotropy of the minority carrier diffusion in the sample. However, there were concerns that the

non-symmetric shape of the luminescence distribution could be a beam related artifact. However, the 3 October 2006 spot image was taken with the series of images shown in Figure 27, which illustrated that the differences in the luminescence distributions were a function of the sample properties only, and not due to any changes in the electron beam from measurement to measurement.

To initially analyze the differences in the diffusion lengths as a function of direction, a Matlab code was created to extract the diffusion length directly from the image. This speeds up the process since the program extracts the line profiles, while previous work with SigmaPlot utilized manual line profile extraction, plotting, and linear regression for slope extraction. Additionally, the Matlab program extracts horizontal, vertical, and  $\pm 45^\circ$  line profiles, analyzes them and outputs the corresponding diffusion lengths. Appendix A contains the Matlab code 'anisotropic.m' which was developed.

For accurate diffusion length values, the Slope Matching method or the T-Factor method needs to be used. These methods both require manual input via model simulation look-ups or graph interpretation. The T-Factor method utilizes Figure 13 to iteratively calculate the diffusion length. A Matlab program using a data file derived from Figure 13 was developed to iteratively compute the diffusion length until the program converged to a value that is within 0.1% of the previous value. This program saves time from manually slope matching or iteratively computing accurate diffusion lengths. Appendix B contains the Matlab function 'Tfactor.m', and Appendix C contains the data file 'Tfactordata.csv' used by the T-Factor function. Figure 30 shows two output graphs produced by the Matlab codes described above. The diffusion length computed by the code is displayed directly in Matlab, and a sample result is shown in Table 6.

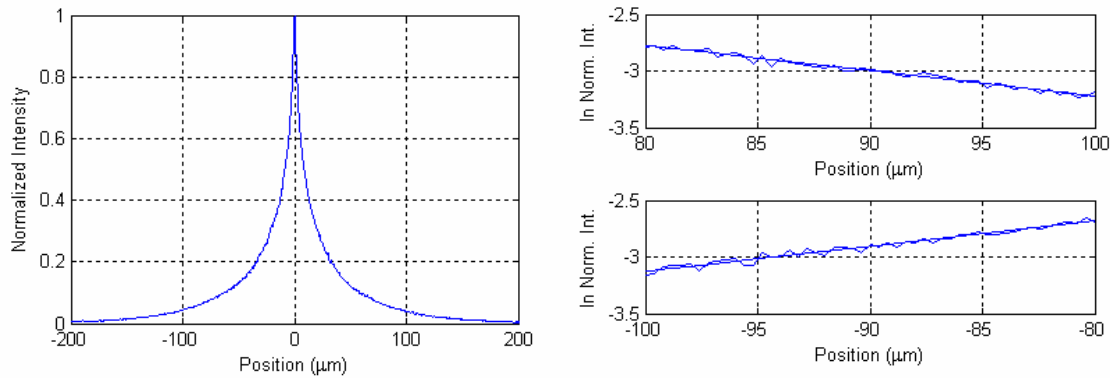


Figure 30. Output Plots of Matlab Code 'anisotropic.m'.

The preliminary results using the Matlab codes show that the InGaP sample does have differing values of diffusion length as a function of crystallographic direction. Table 6 shows the diffusion lengths of the two spot images shown in Figure 29. The results show the diffusion lengths extracted from a horizontal line profile, a vertical line profile, and  $\pm 45^\circ$  line profile. The results show that the diffusion lengths taken from the horizontal line profiles on 28 Sept match the diffusion lengths taken from the vertical line profiles on 3 Oct. Similarly, the diffusion lengths from the 28 Sept vertical line profiles and the 3 Oct horizontal line profiles are also highly reproducible. Both measurements show that the longer diffusion length is 25% greater than the shorter diffusion length.

Sample	Date of Measurement	Diffusion Lengths via T-Factor ( $\mu\text{m}$ )							
		Horizontal Line Profile		Vertical Line Profile		$+45^\circ$ Line Profile		$-45^\circ$ Line Profile	
LM InGaP	9/28/2006	3.2	3.3	3.9	3.9	3.6	3.3	3.4	3.3
LM InGaP	10/3/2006	3.9	4.0	3.2	3.3	3.8	3.7	3.4	3.7

Table 6. Results of Anisotropic Diffusion Length Measurements in InGaP.

As the results show, diffusion lengths can depend on the direction within the semiconductor. This indicates possible crystallographic variations of scattering and/or the effective mass of the minority charge carrier. Future work needs to address this behavior to verify the repeatability of this result and to correlate results with specific crystallographic properties of the sample. This technique would be the most direct measurement of minority carrier transport anisotropy.

## 2. Radiation Effects on Diffusion Length

A key requirement of space rated solar cells is the ability to produce power at the space vehicle's end-of-life (EOL). The radiation environment in space continuously degrades the efficiency of the solar cell, reducing the overall power output of the solar array. This degradation has to be accounted for, and therefore, all satellite power systems are designed to produce the required power at the expected EOL radiation dosage. This increases the size and mass of the solar arrays needed. Solar cells that are radiation resistant will require less solar array area, and therefore less mass, to produce the power required at EOL.

The imaging transport technique can be used to study the material parameter changes as a function of radiation exposure. The changes in diffusion length of the material after radiation damage can show whether or not electrons will be efficiently collected from the cell. This change was illustrated using a small piece of the GaAs sample 24-1Mb. A region of the sample was irradiated with 1.5 MeV protons for 3 seconds. After irradiation, the sample was placed in the SEM and luminescence measurements were taken. Figure 31 shows an image while the SEM was in picture mode. The right hand side of the picture shows the luminescence of the non-radiated GaAs material, while the left hand side shows the radiation damaged region, with dramatically reduced luminescent response.

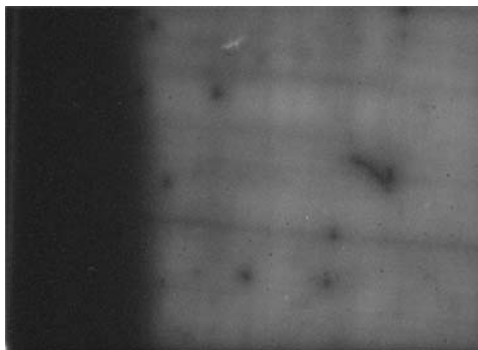


Figure 31. Image ( $700\ \mu\text{m} \times 500\ \mu\text{m}$ ) of Luminescence from Radiation Damaged GaAs with SEM in Picture Mode.

The radiation effects are shown more clearly in the series of images in Figure 32. From left to right, the images are taken in SEM spot mode (electron beam energy of 20 keV, probe current of  $6 \times 10^{-11}$  A, exposure time of 15 seconds) with the beam center fully in the radiation damaged region, on the boundary between the damaged and undamaged regions, and fully in the undamaged region. As previously illustrated in Figure 31, the luminescence intensity in response to spot excitation in Figure 32 is significantly reduced in the radiation damaged regions of the sample, while relatively unchanged in the undamaged regions. This is further illustrated in the line profiles of Figure 33, which show that the intensity decreases as the spot moves from the undamaged region, to the boundary between regions, and increasingly further in the radiation damaged region. Figure 33 shows that the intensity of the luminescence decreases as the spot is moved further into the radiation damaged region under identical excitation parameters and image exposure. Figure 34 is a semi-logarithmic plot of the normalized intensity of the spot image on the boundary. It shows the intensity decrease more quickly on the damaged side, reflected in a change in the slope of the intensity as a function of position.

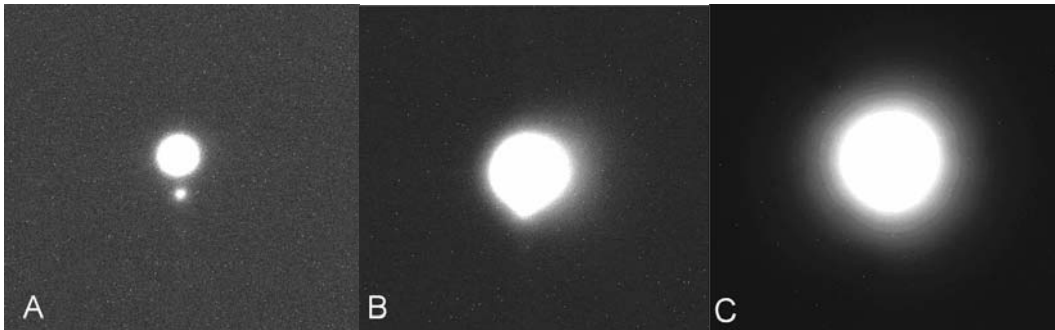


Figure 32. Spot Mode Images ( $216 \mu m \times 200 \mu m$ ) of Luminescence Distribution Changes in Damaged (A), Undamaged (C), and between the Damaged/Undamaged Regions (B) of GaAs.



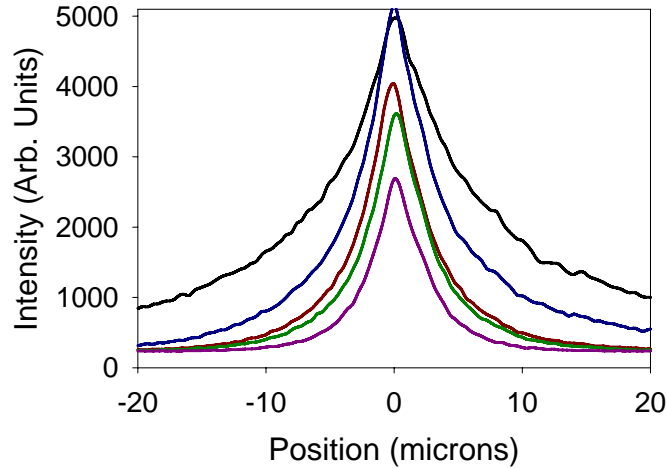


Figure 33. Line Profiles of Spot Images in Undamaged and Radiation Damaged GaAs.

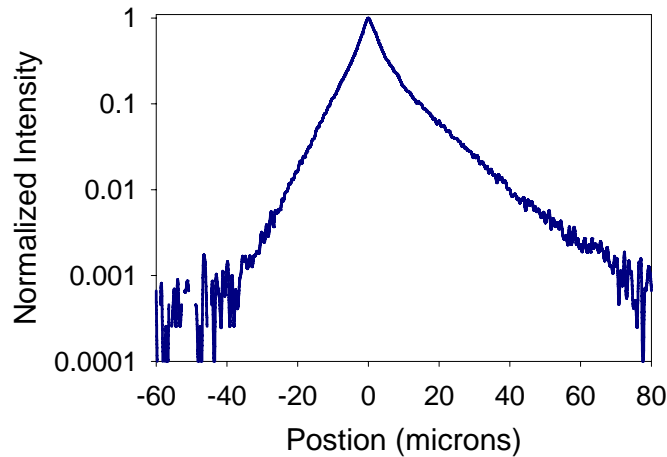


Figure 34. Semi-logarithmic Plot of Normalized Intensity versus Position for Luminescence of Figure 32.B.

Results from the radiation damaged GaAs sample are shown in Table 7. The diffusion lengths extracted via SigmaPlot and the T-factor Matlab function show that the diffusion length is unchanged in the undamaged section of the sample. However, on the boundary between the damaged and undamaged sections, the diffusion length is reduced in both directions. Finally, the diffusion length in the damaged region is only 34% of the diffusion length in the original material.

Sample	Diffusion Lengths via T-Factor ( $\mu\text{m}$ )					
	Damaged Region		Boundary Region		Undamaged Region	
GaAs (24-1Mb)	3.0	3.2	5.9	14.1	17.2	17.0

Table 7. Diffusion Length Measurements of Radiation Damaged GaAs.

The goal of future research in this area would be to incrementally radiation damage a layer of solar cell material, measuring the decrease in diffusion length as a function of radiation damage. This work would be valuable in emerging solar cell technologies, allowing the radiation characteristics of the individual cells to be calculated by providing information on the most fundamental transport parameters. Combined with additional full cell modeling, the total solar cell performance under different radiation dosages can be accurately estimated before the solar cells are grown and assembled.

## APPENDIX A. ANISOTROPIC DIFFUSION LENGTH MEASUREMENT MATLAB CODE (ANISOTROPIC.M)

```

clear all;
close all;
clc;
% set inner and outer slope values
rin=80;
rout=100;
% read tiff, make double precision, find size
Z=imread('1113_23_1Mb2','TIFF');
Z=double(Z);
yx=size(Z);
% create X and Y meshgrid size of Z
xx=linspace(1,yx(2),yx(2));
yy=linspace(1,yx(1),yx(1));
[X,Y] = meshgrid(xx,yy);
%Find spot peak in Z
[YY,II] = max(Z);
[ZMax,Xmax] = max(YY);
Ymax=II(Xmax);
%3-d plot spot
figure(1)
mesh(X,Y,Z)
axis equal
contour(X,Y,Z)
axis equal
axis ([0 max(yx) 0 max(yx)])

% Horizontal Line Profile, 0 degrees from x-axis
% Extract Horizontal line profile, normalize and subtract noise floor
xline=Z(Ymax,:);
xlinenorm=(xline-mean(xline(5:15)))/(ZMax-mean(xline(5:15)));
% Create position vector
xmicron= .4*(xx-Xmax);
% Plot line profile
figure(2)
plot(xmicron,xlinenorm); grid
axis([-rout*2 rout*2 0 1])
xlabel('Position (\mum)');
ylabel('Normalized Intensity');
% Extract slope from line profile, positive microns
mm=1;
for m=1:yx(2)
    if xmicron(m) >= rin & xmicron(m) <=rout
        % Pulls the x_position in microns
        xpos(mm) = xmicron(m);
        % Pulls the Normalized Intensity
        Inormpos(mm) = xlinenorm(m);
        % Increments the counter
        mm=mm+1;
    end
end
% Takes natural log of Normalized Intensity

```

```

Ilnormpos=log(Inormpos);
% Plots ln of Normalized Intensity vs. position
figure(3);
subplot(2,1,1);
plot(xpos,Ilnormpos);grid;hold on;
xlabel('Position (\mum)');
ylabel('ln Norm. Int. ');
% Linear regression of plot, displays Diffusion Length, plots
regression
[P,S] = polyfit(xpos,Ilnormpos,1);
m=P(1);
Ldiff_0_pos=1/abs(m);
Ldiff_0_pos= Tfactor(Ldiff_0_pos, (rout-rin)/2)
b=P(2);
f = @(x)m*x+b;
fplot(f,[rin rout]);
% Extract slope from line profile, negative microns
mm=1;
for m=1:yx(2)
    if xmicron(m) <= -rin & xmicron(m) >= -rout
        % Pulls the x_position in microns
        xneg(mm) = xmicron(m);
        % Pulls the Normalized Intensity
        Inormneg(mm) = xlinenorm(m);
        % Increments the counter
        mm=mm+1;
    end
end
% Takes natural log of Normalized Intensity
Ilnormneg=log(Inormneg);
% Plots ln of Normalized Intensity vs. position
figure(3);
subplot(2,1,2);
plot(xneg,Ilnormneg);grid;hold on;
xlabel('Position (\mum)');
ylabel('ln Norm. Int. ');
% Linear regression of plot, displays Diffusion Length, plots
regression
[P,S] = polyfit(xneg,Ilnormneg,1);
m=P(1);
Ldiff_0_neg=1/abs(m);
Ldiff_0_neg= Tfactor(Ldiff_0_neg, (rout-rin)/2)
b=P(2);
f = @(x)m*x+b;
fplot(f,[-rin -rout]);

% Vertical Line Profile, 90 degrees from x-axis
% Extract line profile, normalize and subtract noise floor
yline=Z(:,Xmax)';
ylinenorm=(yline-mean(yline(5:15)))/(ZMax-mean(yline(5:15)));
% Create position vector
ymicron= .4*(yy-Ymax);
% Plot line profile
figure(4)
plot(ymicron,ylinenorm); grid
axis([-rout*2 rout*2 0 1])
xlabel('Position (\mum)');

```

```

ylabel('Normalized Intensity');
% Extract slope from line profile, positive microns
mm=1;
for m=1:yx(1)
    if ymicron(m) >= rin & ymicron(m) <= rout
        % Pulls the y_position in microns
        ypos(mm) = ymicron(m);
        % Pulls the Normalized Intensity
        Inormpos(mm) = ylinenorm(m);
        % Increments the counter
        mm=mm+1;
    end
end
% Takes natural log of Normalized Intensity
Ilnnormpos=log(Inormpos);
% Plots ln of Normalized Intensity vs. position
figure(5);
subplot(2,1,1);
plot(ypos,Ilnnormpos);grid;hold on;
xlabel('Position (\mum)');
ylabel('ln Norm. Int. ');
% Linear regression of plot, displays Diffusion Length, plots
regression
[P,S] = polyfit(ypos,Ilnnormpos,1);
m=P(1);
Ldiff_90_pos=1/abs(m);
Ldiff_90_pos= Tfactor(Ldiff_90_pos, (rout-rin)/2)
b=P(2);
f = @(x)m*x+b;
fplot(f,[rin rout]);
% Extract slope from line profile, negative microns
mm=1;
for m=1:yx(1)
    if ymicron(m) <= -rin & ymicron(m) >= -rout
        % Pulls the y_position in microns
        yneg(mm) = ymicron(m);
        % Pulls the Normalized Intensity
        Inormneg(mm) = ylinenorm(m);
        % Increments the counter
        mm=mm+1;
    end
end
% Takes natural log of Normalized Intensity
Ilnnormneg=log(Inormneg);
% plots ln of Normalized Intensity vs. position
figure(5);
subplot(2,1,2);
plot(yneg,Ilnnormneg);grid;hold on;
xlabel('Position (\mum)');
ylabel('ln Norm. Int. ');
% Linear regression of plot, displays Diffusion Length, plots
regression
[P,S] = polyfit(yneg,Ilnnormneg,1);
m=P(1);
Ldiff_90_neg=1/abs(m);
Ldiff_90_neg= Tfactor(Ldiff_90_neg, (rout-rin)/2)
b=P(2);

```

```

f = @(x)m*x+b;
fplot(f,[-rin -rout]);

% Extract line profile @ 45 degrees above +x-axis
% Re-initialize variables
xline = 0;
xmicron = 0;
mm=0;
% Find maximum for the 'for' loop below
if (yx(2)-Xmax+1) > Ymax
    mmax = Xmax + Ymax-1;
else
    mmax = yx(2);
end
% Extract half of line profile
for m = Xmax:mmax
    xline(m)=Z(Ymax-mm,m);
    xmicron(m) = sqrt(.32)*(m-Xmax);
    mm = mm + 1;
end
% Re-initialize for other half of line profile extraction
mm = 1;
% Compute min for the 'for' loop below
if Xmax - 1 > yx(1) - Ymax
    mmin = (Xmax-1) - (yx(1) - Ymax) +1;
else
    mmin = 1;
end
% Extract other half of line profile
for m = Xmax-1:-1:mmin
    xline(m)=Z(Ymax+mm,m);
    xmicron(m)=sqrt(.32)*(m-Xmax);
    mm = mm + 1;
end
% Truncate line profile and position vector to get rid of extra zeros
that
% would make noise floor correction incorrect
if mmin ~= 1
    xlinehold = xline;
    xline = 0;
    xline = xlinehold(mmin:mmax);
    xmicronhold = xmicron;
    xmicron = 0;
    xmicron = xmicronhold(mmin:mmax);
end
% Normalize line profile and subtract noise floor
xlinenorm=(xline-mean(xline(5:15)))/(ZMax-mean(xline(5:15)));
% Plot line profile
figure(6)
plot(xmicron,xlinenorm); grid
axis([-rout*2 rout*2 0 1])
xlabel('Position (\mum)');
ylabel('Normalized Intensity');
% Extract slope from line profile, positive microns
mm=1;
xpos = 0;
Inormpos = 0;

```

```

Ilnnormpos = 0;
xneg = 0;
Inormneg = 0;
Ilnnormneg = 0;
[my mx] = size(xmicron);
for m=1:mx
    % Checks to see if we are in slope extraction range
    if xmicron(m) >= rin & xmicron(m) <=rout
        % Pulls the x_position in microns
        xpos(mm) = xmicron(m);
        % Pulls the Normalized Intensity
        Inormpos(mm) = xlinenorm(m);
        % Increments the counter
        mm=mm+1;
    end
end
% Takes natural log of Normalized Intensity
Ilnnormpos=log(Inormpos);
% Plots ln of Normalized Intensity vs. position
figure(7);
subplot(2,1,1);
plot(xpos,Ilnnormpos);grid;hold on;
xlabel('Position (\mum)');
ylabel('ln Norm. Int. ');
% Linear regression of plot, displays Diffusion Length, plots
regression
[P,S] = polyfit(xpos,Ilnnormpos,1);
m=P(1);
Ldiff_p45_pos=1/abs(m);
Ldiff_p45_pos= Tfactor(Ldiff_p45_pos, (rout-rin)/2)
b=P(2);
f = @(x)m*x+b;
fplot(f,[rin rout]);
% Extract slope from line profile, neg microns
mm=1;
for m=1:mx
    % Checks to see if we are in slope extraction range
    if xmicron(m) <= -rin & xmicron(m) >= -rout
        % Pulls the x_position in microns
        xneg(mm) = xmicron(m);
        % Pulls the Normalized Intensity
        Inormneg(mm) = xlinenorm(m);
        % Increments the counter
        mm=mm+1;
    end
end
% Takes natural log of Normalized Intensity
Ilnnormneg=log(Inormneg);
% Plots ln of Normalized Intensity vs. position
figure(7);
subplot(2,1,2);
plot(xneg,Ilnnormneg);grid;hold on;
xlabel('Position (\mum)');
ylabel('ln Norm. Int. ');
% Linear regression of plot, displays Diffusion Length, plots
regression
[P,S] = polyfit(xneg,Ilnnormneg,1);

```

```

m=P(1);
Ldiff_p45_neg=1/abs(m);
Ldiff_p45_neg= Tfactor(Ldiff_p45_neg, (rout-rin)/2)
b=P(2);
f = @(x)m*x+b;
fplot(f,[-rin -rout]);

% Extract line profile @ 45 degrees below +x-axis
% Re-initialize variables
xline = 0;
xmicron = 0;
mm=0;
% Find maximum for the 'for' loop below
if (yx(2)-Xmax+1) > yx(1) - Ymax+1
    mmax = Xmax + yx(1) - Ymax;
else
    mmax = yx(2);
end
% Extract half of line profile
for m = Xmax:mmax
    xline(m)=Z(Ymax+mm,m);
    xmicron(m) = sqrt(.32)*(m-Xmax);
    mm = mm + 1;
end
% Re-initialize for other half of line profile extraction
mm = 1;
% Compute min for the 'for' loop below
if Xmax - 1 > Ymax -1
    mmin = (Xmax-1) - Ymax + 2;
else
    mmin = 1;
end
% Extract other half of line profile
for m = Xmax-1:-1:mmin
    xline(m)=Z(Ymax-mm,m);
    xmicron(m)=sqrt(.32)*(m-Xmax);
    mm = mm + 1;
end
% Truncate line profile and position vector to get rid of extra zeros
that
% would make noise floor correction incorrect
if mmin ~= 1
    xlinehold = xline;
    xline = 0;
    xline = xlinehold(mmin:mmax);
    xmicronhold = xmicron;
    xmicron = 0;
    xmicron = xmicronhold(mmin:mmax);
end
% Normalize line profile and subtract noise floor
xlinenorm=(xline-mean(xline(5:15)))/(ZMax-mean(xline(5:15)));
% Plot line profile
figure(8)
plot(xmicron,xlinenorm); grid
axis([-rout*2 rout*2 0 1])
xlabel('Position (\mu m)');
ylabel('Normalized Intensity');

```



```

% Extract slope from line profile, positive microns
mm=1;
xpos = 0;
Inormpos = 0;
Ilnnormpos = 0;
xneg = 0;
Inormneg = 0;
Ilnnormneg = 0;
[my mx] = size(xmicron);
for m=1:mx
    % Checks to see if we are in slope extraction range
    if xmicron(m) >= rin & xmicron(m) <=rout
        % Pulls the x_position in microns
        xpos(mm) = xmicron(m);
        % Pulls the Normalized Intensity
        Inormpos(mm) = xlinenorm(m);
        % Increments the counter
        mm=mm+1;
    end
end
% Takes natural log of Normalized Intensity
Ilnnormpos=log(Inormpos);
% Plots ln of Normalized Intensity vs. position
figure(9);
subplot(2,1,1);
plot(xpos,Ilnnormpos);grid;hold on;
xlabel('Position (\mum)');
ylabel('ln Norm. Int. ');
% Linear regression of plot, displays Diffusion Length, plots
regression
[P,S] = polyfit(xpos,Ilnnormpos,1);
m=P(1);
Ldiff_n45_pos=1/abs(m);
Ldiff_n45_pos= Tfactor(Ldiff_n45_pos, (rout-rin)/2)
b=P(2);
f = @(x)m*x+b;
fplot(f,[rin rout]);
% Extract slope from line profile, neg microns
mm=1;
for m=1:mx
    % Checks to see if we are in slope extraction range
    if xmicron(m) <= -rin & xmicron(m) >= -rout
        % Pulls the x_position in microns
        xneg(mm) = xmicron(m);
        % Pulls the Normalized Intensity
        Inormneg(mm) = xlinenorm(m);
        % Increments the counter
        mm=mm+1;
    end
end
% Takes natural log of Normalized Intensity
Ilnnormneg=log(Inormneg);
% Plots ln of Normalized Intensity vs. position
figure(9);
subplot(2,1,2);
plot(xneg,Ilnnormneg);grid;hold on;
xlabel('Position (\mum)');

```

```

ylabel('ln Norm. Int. ');
% Linear regression of plot, displays Diffusion Length, plots
regression
[P,S] = polyfit(xneg,Ilnnormneg,1);
m=P(1);
Ldiff_n45_neg=1/abs(m);
Ldiff_n45_neg= Tfactor(Ldiff_n45_neg, (rout-rin)/2)
b=P(2);
f = @(x)m*x+b;
fplot(f,[-rin -rout]);

```

## APPENDIX B. T-FACTOR DIFFUSION LENGTH MEASUREMENT MATLAB FUNCTION (TFACOR.M)

```
function Lact=Tfactor(Lest, xm);
data = csvread('tfactordata.csv');
[m n] = size(data);
Lact = Lest;
L = .01;
while abs((Lact-L)/L) > 0.001;
    xmoverL=xm/Lact;
    L = Lact;
    for k=1:m
        if xmoverL < data(k,1)
            Lact=Lest/data(k,2);
            k=m;
        end
    end
end
end
```

THIS PAGE INTENTIONALLY LEFT BLANK

## APPENDIX C. T-FACTOR DIFFUSION LENGTH MEASUREMENT DATA FILE (TFACTORDATA.CSV)

5.00,0.9130  
4.95,0.9125  
4.90,0.9120  
4.85,0.9110  
4.80,0.9105  
4.75,0.9095  
4.70,0.9085  
4.65,0.9075  
4.60,0.9070  
4.55,0.9060  
4.50,0.9050  
4.45,0.9040  
4.40,0.9030  
4.35,0.9025  
4.30,0.9015  
4.25,0.9005  
4.20,0.8995  
4.15,0.8985  
4.10,0.8970  
4.05,0.8960  
4.00,0.8950  
3.95,0.8940  
3.90,0.8930  
3.85,0.8915  
3.80,0.8905  
3.75,0.8890  
3.70,0.8880  
3.65,0.8865  
3.60,0.8855  
3.55,0.8840  
3.50,0.8825  
3.45,0.8810  
3.40,0.8800  
3.35,0.8785  
3.30,0.8770  
3.25,0.8755  
3.20,0.8735  
3.15,0.8720  
3.10,0.8705  
3.05,0.8685  
3.00,0.8670  
2.95,0.8650  
2.90,0.8630  
2.85,0.8615  
2.80,0.8595  
2.75,0.8575  
2.70,0.8550  
2.65,0.8530  
2.60,0.8510  
2.55,0.8485  
2.50,0.8460

2.45,0.8435  
2.40,0.8410  
2.35,0.8385  
2.30,0.8360  
2.25,0.8330  
2.20,0.8305  
2.15,0.8275  
2.10,0.8240  
2.05,0.8210  
2.00,0.8180  
1.95,0.8140  
1.90,0.8110  
1.85,0.8070  
1.80,0.8030  
1.75,0.7990  
1.70,0.7950  
1.65,0.7910  
1.60,0.7860  
1.55,0.7810  
1.50,0.7760  
1.45,0.7710  
1.40,0.7650  
1.35,0.7590  
1.30,0.7530  
1.25,0.7470  
1.20,0.7400  
1.15,0.7320  
1.10,0.7250  
1.05,0.7170  
1.00,0.7090

## LIST OF REFERENCES

1. Kasap, S.O., *Principles of Electronic Materials and Devices*, Second Edition (McGraw-Hill, New York, 2002).
2. Larsen, W.J. and J.R. Wertz, editors, *Space Mission Analysis and Design*, Third Edition (Microcosm Press, El Segundo, California, 1999).
3. *Data Sheet, 28.3% Ultra Triple Junction (UTJ) Solar Cells*. 6 Apr 2006. Spectrolab, Inc. 2 December 2006  
<<http://www.spectrolab.com/DataSheets/TNJCell/utj3.pdf>>.
4. Michael, S., "Space Power and Radiation Effects" Course Notes, Naval Postgraduate School, Monterey, California, March 2006.
5. Kasap, S.O., *Optoelectronics and Photonics, Principles and Practices* (Prentice Hall, New Jersey, 2001).
6. Ito, H. and T. Ishibashi, *Journal of Applied Physics* **65**, 12 (1989).
7. Haynes, J.R. and W. Shockley, *Physical Review* **85**, 835 (1951).
8. Haegel, N.M., J.D. Fabbri and M.P. Coleman, *Applied Physics Letters* **84**, 8 (2004).
9. Luber, D.R., F.M. Bradley, N.M. Haegel, M.C. Talmadge, M.P. Coleman and T.D. Boone, *Applied Physics Letters* **88**, 163509 (2006).
10. Boaz, M.L., *Mathematical Methods in the Physical Sciences*, Second Edition (John Wiley and Sons, 1983).
11. Talmadge, M. *Zero Bias Diffusion Length Extraction*, Memo to Naval Postgraduate School (Fairfield University, Connecticut, 2005).
12. Winchell, S., *Transport Imaging in the One Dimensional Limit*, Master's Thesis, Naval Postgraduate School, Monterey, California, June 2006.
13. Goldstein, J., D. Newbury, D. Joy, C. Lyman, P. Echlin, E. Lifshin, L. Sawyer and J. Michael, *Scanning Electron Microscopy and X-Ray Microanalysis*, Third Edition (Plenum, New York, 2002).
14. Dabkowski, F.P., P. Gavrilovic, K. Meehan, W. Stutius, J.E. Williams, M.A. Shahid and S. Mahajan, *Applied Physics Letters* **52**, 25 (1988).
15. Dobročka, E., I. Vávra and L.R. Wallenberg, *Journal of Applied Physics* **89**, 5 (2001).

16. Romero, M.J., D. Araújo, R. García, R.J. Walters, G.P. Summers and S.R. Messenger, *Applied Physics Letters* **74**, 18 (1999).
17. Lee, M.K., R.H. Horng, and L.C. Haung, *Applied Physics Letters* **59**, 25 (1991).
18. Sze, S.M., *Physics of Semiconductor Devices*, Second Edition (John Wiley & Sons, New York, 1981).
19. Ito, H. and T. Ishibashi, *Journal of Applied Physics* **65**, 12 (1989).



## INITIAL DISTRIBUTION LIST

1. Defense Technical Information Center  
Ft. Belvoir, Virginia
2. Dudley Knox Library  
Naval Postgraduate School  
Monterey, California
3. Professor James H. Luscombe  
Naval Postgraduate School  
Monterey, California
4. Professor Nancy M. Haegel  
Naval Postgraduate School  
Monterey, California
5. Professor Sherif Michael  
Naval Postgraduate School  
Monterey, California
6. Ted Jonathan Mills  
AFELM DSPO DO  
Washington, DC
7. Nasser H. Karam  
Spectrolab, Inc.  
Sylmar, California
8. Richard R. King  
Spectrolab, Inc.  
Sylmar, California
9. Hojun Yoon  
Spectrolab, Inc.  
Sylmar, California
10. David R. Luber  
Headquarters United States Marine Corps  
Sylmar, California
11. Kin Man Yu  
Lawrence Berkeley National Laboratory  
Berkeley, California